NANO-SCALE PLASMONIC RESONATORS FOR BIO-SENSING

BY

MOHAMMED TAYYAB MOHI MUJAHID

A Thesis Presented to the
DEANSHIP OF GRADUATE STUDIES

KING FAHD UNIVERSITY OF PETROLEUM & MINERALS
DHAHRAN, SAUDI ARABIA

In Partial Fulfillment of the
Requirements for the Degree of

MASTER OF SCIENCE

In

ELECTRICAL ENGINEERING

DECEMBER 2013

KING FAHD UNIVERSITY OF PETROLEUM & MINERALS

DHAHRAN- 31261, SAUDI ARABIA

DEANSHIP OF GRADUATE STUDIES

This thesis, written by **MOHAMMED TAYYAB MOHI MUJAHID** under the direction his thesis advisor and approved by his thesis committee, has been presented and accepted by the Dean of Graduate Studies, in partial fulfillment of the requirements for the degree of **MASTER OF SCIENCE IN ELECTRICAL ENGINEERING.**

Dr. Mohammad A. Alsunaidi
(Advisor)

Dr. Ali Ahmad Al-Shaikhi
Department Chairman

Dr. Hussain Ali Al-Jamid
(Member)

Dr. Salam A. Zummo
Dean of Graduate Studies

Dr. Nabil Maalej
(Member)

9/1/14
Date

-

Dedicated to my

Parents, siblings and their sacrifices

ACKNOWLEDGMENTS

All praise, glory and gratitude is for Allah, the most beneficent, the most merciful

I thank my advisor Dr. Mohammed Alsunaidi for introducing me to the field of plasmonics to which I was bliss-fully unaware and also rekindling my interest in electromagnetics. Working with him was very enlightening experience and I consider him one of the few people who have shaped my outlook and attitude towards research and life in general. I also thank him for all the support, encouragement, suggestions and bearing with me with his infinite reserves of patience.

I would like to thank my committee members Dr. Hussain Ali Jamid and Dr. Nabil Maalej for their valuable suggestions, positive feedback and investing their valuable time to be part of my thesis committee.

I'm grateful to my friends here at KFUPM and also group members Zia and Waqas.

I would also like to thank KFUPM for providing world class facilities and their support throughout my stay here in Saudi Arabia

TABLE OF CONTENTS

LIST OF TABLES

LIST OF FIGURES

LIST OF ABBREVIATIONS

FDTD: – Finite Difference Time Domain

TFSF: – Total Field/Scattered Field

FWHM: –Full Wave Half Maximum

FOM: – Figure of Merit

LOD: –Limit of Detection

RIU: – Refractive Index Units

MI PML: –Material Independent Perfectly Matched Layer

ABSTRACT

Full Name : Mohammed Tayyab Mohi Mujahid
Thesis Title : Nano-scale Plasmonic Resonators for Bio-sensing
Major Field : Electrical Engineering
Date of Degree : December, 2013

Plasmonic bio-sensors are among the most sensitive bio-sensing devices. Plasmonics has been used in a range of spectroscopic methods and binding analysis techniques for enhancing sensitivity, resolution and limit of detection.

This thesis utilizes multiple sensitivities in the design of bio-sensors. Two types of structures have been investigated; one with passive components and the other with active components. The passive plasmonic devices are based on the Metal-Insulator-Metal waveguide coupled ring resonator structure. The inherent sensitivity of the ring resonator and the delicate nature of the surface plasmon wave gave rise to an enhanced overall sensitivity to changes in refractive index of the bio-material and the introduction of grating gave the ability to tune the response of the device and reduce its size.

The active device design is based on an emitter coupled to plasmonic nano-particles. This design utilized the narrow emission spectrum of the active media and the narrow response of plasmonic nano-particles. This gave an over-all enhanced sensitivity of intensity enhancement close to the nano-particles to changes in refractive index of the bio-material. The analysis is based on a time-domain simulator that incorporates material properties using Finite-Difference Time-Domain (FDTD) method.

ملخص الرسالة

الاسم الكامل: محمد طيب محى مجاهد

عنوان الرسالة: الإستشعار الحيوي باستخدام التشكيلات البلازمية متناهية الصغر

التخصص: الهندسه الكربائيه

تاريخ الدرجة العلمية: ديسمبر، 2013

أجهزة الاستشعار البيولوجية البلازمية هي من بين الأجهزة الأكثر حساسية للاستشعار الحيوي. وقد تم استخدام البلازما في مجموعة من الطرق الطيفية لتعزيز الحساسية، الوضوح، وتحديد مدى الكشف. بعض الطرق الطيفية الشائعة التي استخدمت البلازما هي طيف تعزيز سطوح رامان (SERS)، طيف تعزيز السطوح تحت الحمراء (SEIRS) وأجهزة الاستشعار المتقاربة.

في هذه الأطروحة تم اقتراح الاستفادة من الحساسيات المتعددة في تصميم أجهزة الاستشعار الحيوي. وهناك نموذجان تم أخذهما بعين الاعتبار؛ الأول باستخدام العناصر غير المتفاعلة والآخر باستخدام العناصر المتفاعلة. جهاز البلازما غير المتفاعل يعتمد على نموذج التردد الدائري. الحساسية المتأصلة في حلقة الرنين والطبيعة الحساسة لموجة البلازما السطحية أعطت زيادة للحساسية الكلية المعززة. وبالنسبة للنموذج المتفاعل تم تصميمه بالاعتماد على الاستفادة من طيف الانبعاث الضيق للوسائط النشطة للحصول على حساسية معززة لترددات البلازما ذات الجسيمات المتناهية الصغر. ويعتمد التحليل في هذه الرسالة على برنامج محاكاة مستند على المجال الزمني والذي يشتمل على خصائص المواد. وتم إيجاد الحل العددي باستخدام طريقة (FDTD).

1. Chapter 1

INTRODUCTION

The electrons close to metal surfaces (called surface plasma) can perform coherent fluctuations when excited by a properly polarized light [1]. These fluctuations are called surface plasmons (quantum equivalent of plasma) resonances. Surface plasmon resonances can be excited either on plane metallic surfaces or in metal nano particles. When surface plasmons are excited in a metal nanoparticle they are called localized surface plasmon resonances (LSPR). There is a drastic alteration in the incident electromagnetic wave when a surface plasmon is excited. This ability of light makes it immune to the diffraction limit and light can now be manipulated at sub-wavelength volumes.

Some of the most important and early demonstrations of manipulation of light at sub-wavelength scale using surface plasmons was done by Thomas Ebbesens's [2] extraordinary optical transmission through sub-wavelength apertures and John Pendry's [3] suggestion of using a metallic film as a "perfect lens". This led to a huge interest in research in plasmonics and its applications. This ability of surface plasmons opened up new avenues of research and also gave an understanding of ability to miniaturize photonic components and fabricate 'exotic' material. Apart from applications of plasmonics, the study of optical phenomenon like interferometry, Fano resonance, diffraction, surface plasmon lasing -to name a few - has also been a subject of intense research. The fact that excitation of surface plasmons is dependent on the property of the metal and the environment close to the surface of the metal can be exploited and used in various applications ranging from bio-sensing, lasers, LEDs and photonic integrated circuits. Though the promise of plasmonics until now has not been fulfilled in certain areas but one area which has greatly advanced and immensely matured in its applications and usage is bio-sensing and in particular label-free detection of the chemical reactions and bio-molecular interactions at nano-scale level. This has also led to successful commercialization of such sensors.

1.1 Overview of plasmonic bio-sensing

Sensing with using surface plasmons is possible due to strong fields confined to sub-wavelength volumes at metal surfaces. Conventional plasmonic sensors which are generally referred to as surface plasmon resonance (SPR) sensors are based on exciting a propagating mode of surface plasmon along the interface of a film of gold and dielectric material.

Late 1970s and early 1980s saw the development of these types of sensors and it was in 1990 that the first commercial SPR sensor was launched by BIACore Inc. This has led to an increase in demand for extremely sensitively instruments studying such bio-molecular interactions down to the molecular level and has led to rapid development of SPR techniques. To mention a few, SPR sensors have been used in drug-discovery, environmental monitoring, analytical chemistry and medical diagnostics but the area of drug-discovery has been in the forefront in using it.

Proteins give structure to cell and perform most of the cellular functions. Proteins are generally formed from multiple amino acids (20 in types) stringed together. They can range from 100-1000 amino acids in length. Insulin, hemoglobin, antibodies, immunoglobin and DNA molecule are all types of proteins. Antibodies form the basis of the human immune system and they can recognize and bind to specific molecular targets from a huge array of non-specific targets analogous to the “lock-and-key” specificity.

The most common class of anti-body is the Immunoglobin G (IgG) [4]. These have a ‘Y’ structure with two heavy chains and two light chains of amino acids as seen in Figure 1-1. It has three domains. The F_a and F_b branching domains and a central domain. The branched domains are active sites of target (antigen) binding. In an immunoassay the antibodies are anchored to a substrate leaving the active branches of the antibodies for specific binding.

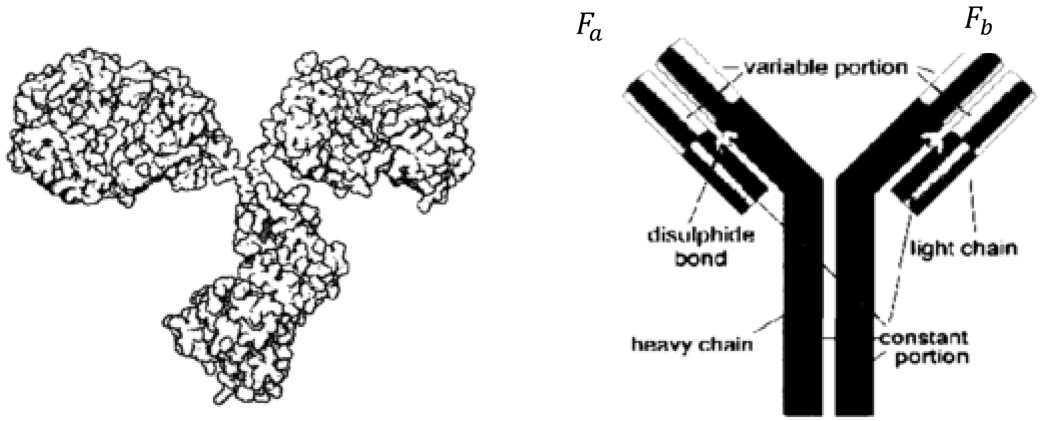

Figure 1-1 Immunoglobin G(IgG) (adapted from [5]**)**

A common immunoassay method is ELISA (Enzyme Linked Immunosorbant Assay). This method uses a secondary enzyme linked antibody for the amplification of the signal. The secondary enzyme can generally be a dye molecule, this is called labeling.

Depending on the technique the label can be a radioisotope, flourophore or an enzyme as shown in Figure 1-2

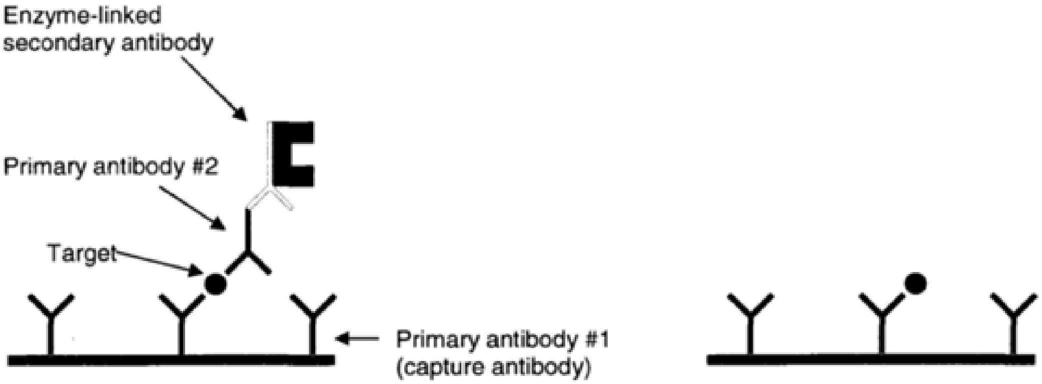

Figure 1-2 ELISA and Label Free sensing (adapted from [5]**)**

However these labels modify the target and remove it from its native state. So label free techniques are used for such situations and SPR sensors come in the picture. SPR sensors allow continuous measurements of the target concentration on the sensor using refractive index changes and allow a real-time analysis of binding kinetics. Label-free techniques are simpler as they require only a single antibody for capture and signaling.

Most of the available SPR sensors use the Kretschmann configuration and are based on attenuated total reflection but various other SPR sensor configurations have been used like phase sensitive SPR sensor, grating based SPR sensor, waveguide excited SPR sensor and fiber-optic excited SPR sensor.

Due to advancements in fabrication and synthesis technologies precise control of metal nano-structures with sizes and features comparable to the wavelength of light and smaller became easy to fabricate. In these nano-particles LSPR can be excited which gives advantages of much higher field enhancements than planar SPR; also the response became wavelength specific depending on the size and shapes of the particle whose response change with refractive index of the surrounding medium.

These two methods would be discussed in detail in the following sections. The conditions for exciting a surface plasmon at the interface between metal and a dielectric are also discussed.

1.2 Analysis of Surface plasmon Sensing

Surface plasmons cannot be directly excited on a flat metal /dielectric interface by light beams because the plasmon propagation constant (β_{sp}) is greater than the wave-vector of light on the dielectric's side of the interface. Therefore to match the propagation constants a prism is used and the light beam is made to excite at a particular angle so that the wave-vector along the direction of propagation is matched to that of the surface plasmon that is excited (β_{sp}).

Surface plasmon that is excited on the interface between a metal and a dielectric interface is an electromagnetic wave with an evanescent decay of fields on both sides of the interface. The general conditions for exciting a surface plasmon at the interface between metal and a dielectric are as follows

1. Incident light is TM polarized.
2. The dielectric constants of metal and the dielectric material satisfy

   $Re\{\varepsilon_m\} < -\varepsilon_d$
3. The wave-vector of the incident light is large enough to satisfy the momentum matching condition $k_x = \beta_{sp}$.

The surface plasmons that are excited on a metal insulator/dielectric interface are evanescently confined in the perpendicular direction. The electromagnetic waves as mentioned before couple to the metal electron plasma near the surface forming one of the simplest forms of surface plasmons.

The dispersion relation of surface plasmons propagating at the interface between metal and dielectric is given by [6]

$$\beta_{sp} = k_o \sqrt{\frac{\varepsilon_d \varepsilon_m}{\varepsilon_d + \varepsilon_m}} \qquad 1.1$$

where β_{sp} is propagation constant of the surface plasmon, k_o is free space propagation constant of the incident light, ε_d is relative permittivity of the dielectric and ε_m is relative permittivity of the metal.

Surface plasmons are extremely sensitive to the relative permittivity of the dielectric material. In a basic SPR sensor the surface plasmon is excited using a prism to match the momentum of the incident electromagnetic wave. When a surface plasmon is excited there is a dip in the reflectivity measured at the detector and the angle at which this dip is measured is a function of change in permittivity of the dielectric.

If excited by a prism the matching condition is

$$\frac{2\pi}{\lambda} n_p \sin\theta = Re\{\beta_{sp}\} \qquad 1.2$$

where n_p is the refractive index of the prism used , θ is the angle of the incidence of the light wave on the metal-prism interface.

The mismatch in the wave-vector and the propagation constant can also be bridged by patterning the metal with holes or groves having a lattice constant (or period) Λ. The following equation shows the relation between the lattice constant and the propagation constant of the surface plasmon.

$$k \sin\theta + m.g = \pm\, Re\{\beta_{sp}\} \qquad 1.3$$

or

$$\frac{2\pi}{\lambda} n_d \sin\theta + m\frac{2\pi}{\Lambda} = \pm Re\{\beta_{sp}\} \qquad 1.4$$

where λ is wavelength of the incident light, n_p is refractive index of the prism, β_{sp} is propagation constant of the supported surface-plasmon. Λ is the period of the grating and m is a positive integer.

If it is excited by a fiber-optic waveguide then the propagation constant of the photonic mode must be matched with that of the propagation constant of the surface plasmon. This method of excitation is highly efficient and the surface plasmons excited by this method are more bounded. The equation 1.5 gives the matching condition.

$$\beta_{mode} = Re\,\{\beta_{sp}\} \qquad 1.5$$

where β_{mode} is the propagation constant of the photonic mode of the optical fiber. Figure 1-3(a) shows the schematic of a Kretschmann configuration for exciting surface plasmons, which uses a prism (of refractive index n_p) and a source of light which can tune the angle of incidence to θ for matching the momentum (equation-1.2) of incident light to that of the surface plasmons excited on the Metal-Biomaterial interface. Figure 1-3(b) shows schematic of how the reflectivity dip changes with change in permittivity of the dielectric (bio-material) thus measuring the changes in the bio-material. This dip in reflectivity is transformed into binding kinetics curves in real time as seen in Figure 1-3(c). The binding kinetics curves plots the output power or signal strength with changes in permittivity with time. These curves are used to find the rate at which binding takes place.

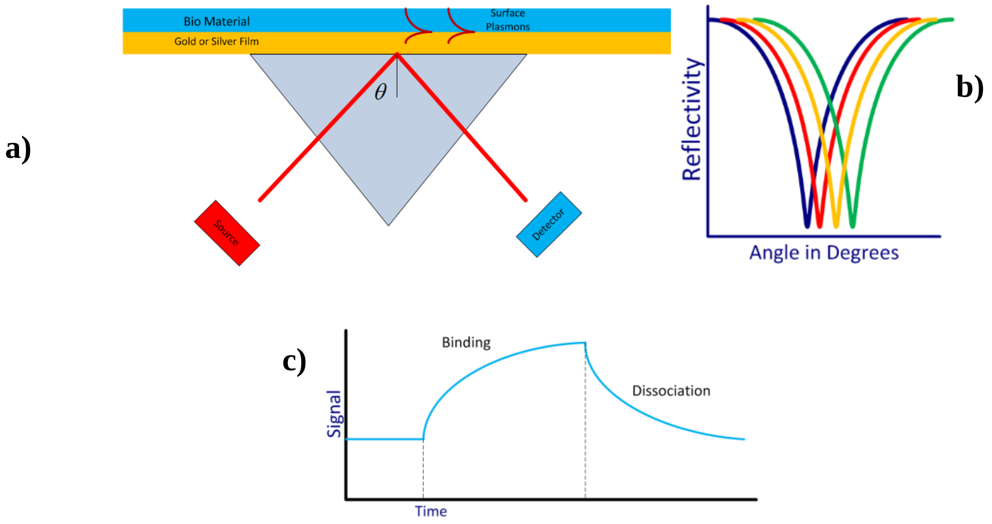

Figure 1-3 a) SP coupling using a prism b) Schematic of reflectivity change with change in permittivity. c) Real -Time binding schematic.

1.2.1 SPR analysis

The surface plasmons that are excited on a metal insulator/dielectric interface are evanescently confined in the perpendicular direction. The electromagnetic waves as mentioned before couple to the metal electron plasma near the surface and are one of the simplest forms of surface plasmons.

An electromagnetic analysis using Maxwell’s equation can be done to help find a closed form solution of surface plasmon modes which can exist.

Maxwell's equations are given by

$$\nabla \times \mathbf{E} = -\frac{\partial \mathbf{B}}{\partial t} \qquad 1.6$$

$$\nabla \times \mathbf{H} = \mathbf{J}_{ext} + \frac{\partial \mathbf{D}}{\partial t} \qquad 1.7$$

$$\nabla . \mathbf{D} = \rho_{ext} \qquad 1.8$$

$$\nabla . \mathbf{B} = 0 \qquad 1.9$$

where, **E** is the electric field vector in volt per meter (V/m)

D is the electric flux density vector in coulombs per square meter (C/m^2)

H is the magnetic field vector in amperes per meter (A/m)

B is the magnetic flux density vector in webbers per square meter $\left(\frac{Wb}{m^2}\right)$

ρ_{ext} is the charge density (C/m^3)

$\boldsymbol{J}_{ext}$ is the external current density (A/m^2)

The relation between electric and magnetic fields with polarization $\boldsymbol{P}$ and magnetization $\boldsymbol{M}$ is given by the following equation.

$$\boldsymbol{D} = \varepsilon_o \boldsymbol{E} + \boldsymbol{P} \qquad 1.10$$

$$\boldsymbol{H} = \frac{1}{\mu_o} \boldsymbol{B} - \boldsymbol{M} \qquad 1.11$$

The electromagnetic wave equation is derived using the Maxwell's equation. For a case of no external charge and current density the equations 1.6-1.9 can be written as

$$\nabla . \boldsymbol{D} = 0 \qquad 1.12$$

$$\nabla \times \nabla \times \boldsymbol{E} = -\mu_o \frac{\partial^2 \boldsymbol{D}}{\partial t^2} \qquad 1.13$$

Using the vector identities of $\nabla \times \nabla \times E = \nabla(\nabla . E) - \nabla^2 E$ and $\nabla . (\varepsilon E) = E . \nabla \varepsilon + \varepsilon \nabla . E$ Equation 1.13 can be written for an isotropic medium case as.

$$\nabla^2 \boldsymbol{E} - \frac{\varepsilon}{c^2} \frac{\partial^2 \boldsymbol{E}}{\partial t^2} = 0 \qquad 1.14$$

Equation 1.14 should be solved using the appropriate boundary conditions. For a time-harmonic electric field$(E(r,t) = E(r)e^{-j\omega t})$ Maxwell's equations can be simplified and written as

$$\nabla^2 \boldsymbol{E} + k^2 \varepsilon \boldsymbol{E} = 0 \qquad 1.15$$

where k is the wave-vector of propagation given by $k = \frac{\omega}{c}$

It is also assumed here that the wave travels along x-direction and there is no spatial variation in y-direction shown in the Figure 1-4. So, from assumption taken before, the electric field can be written as $E(x,y,z) = E(z)e^{j\beta x}$ where $\beta = k_x$ is called the propagation constant. Substituting this expression of electric field in equation 1.15 would give the wave-equation.

$$\frac{\partial^2 \boldsymbol{E}(z)}{\partial t^2} + (k_o^2 \varepsilon - \beta) \boldsymbol{E} = 0 \qquad 1.16$$

Similarly for the magnetic field the wave-equation can be derived and is given by

$$\frac{\partial^2 \boldsymbol{H}(z)}{\partial t^2} + (k_o^2 \varepsilon - \beta) \boldsymbol{H} = 0 \qquad 1.17$$

In Cartesian co-ordinate system the fields can be written as

$$\boldsymbol{E} = E_x a_x + E_y a_y + E_z a_z \qquad 1.18$$

$$\boldsymbol{H} = H_x a_x + H_y a_y + H_z a_z$$

By solving Ampere's and Faraday's law using a time-harmonic field values ($\frac{\partial}{\partial t} = -j\omega$) the following set of coupled equations is obtained

$$\frac{\partial E_z}{\partial y} - \frac{\partial E_y}{\partial z} = j\omega\mu_o H_x \qquad 1.19$$

$$\frac{\partial E_x}{\partial z} - \frac{\partial E_z}{\partial x} = j\omega\mu_o H_y \qquad 1.20$$

$$\frac{\partial E_y}{\partial x} - \frac{\partial E_x}{\partial y} = j\omega\mu_o H_z \qquad 1.21$$

$$\frac{\partial H_z}{\partial y} - \frac{\partial H_y}{\partial z} = -j\omega\varepsilon E_x \qquad 1.22$$

$$\frac{\partial H_x}{\partial z} - \frac{\partial H_z}{\partial x} = -j\omega\varepsilon E_y \qquad 1.23$$

$$\frac{\partial H_y}{\partial x} - \frac{\partial H_x}{\partial y} = -j\omega\varepsilon E_z \qquad 1.24$$

With propagation assumed to be along x-direction $\frac{\partial}{\partial x} = j\beta$ and also with no spatial variation along y-direction results in $\frac{\partial}{\partial y} = 0$. Then the above system of equation simplifies to

$$-\frac{\partial E_y}{\partial z} = j\omega\mu_o H_x \qquad 1.25$$

$$\frac{\partial E_x}{\partial z} - j\beta E_z = j\omega\mu_o H_y \qquad 1.26$$

$$j\beta E_y = j\omega\mu_o H_z \qquad 1.27$$

$$\frac{\partial H_y}{\partial z} = j\omega\varepsilon E_x \qquad 1.28$$

$$\frac{\partial H_x}{\partial z} - j\beta H_z = -j\omega\varepsilon E_y \qquad 1.29$$

$$j\beta H_y = -j\omega\varepsilon E_z \qquad 1.30$$

The above set of equations can be solved for two polarizations with regard to the direction of the electric field i.e. the Transverse Magnetic (TM) and the Transverse Electric (TE).

For the TE polarization the field equations and the wave-equation derived from the above set of equations 1.25-1.30 are given by

$$H_x = j\frac{1}{\mu_o\omega}\frac{\partial E_y}{\partial z} \qquad 1.31$$

$$H_z = \frac{\beta}{\omega\mu_o}E_y \qquad 1.32$$

$$\frac{\partial^2 E_y}{\partial z^2} + (k_o\varepsilon - \beta)E_y = 0 \qquad 1.33$$

For the TM polarization the field equations and the wave equation derived from the above set of equations (1.25-1.30) are given by

$$E_x = -j\frac{1}{\omega\varepsilon}\frac{\partial H_y}{\partial z} \qquad 1.34$$

$$E_z = -\frac{\beta}{\omega\varepsilon}H_y \qquad 1.35$$

$$\frac{\partial^2 H}{\partial z^2} + (k_o\varepsilon - \beta)H_y = 0 \qquad 1.36$$

These equations are used to solve for modes of surface plasmons at various configurations of planar metal – dielectric interfaces when applied with proper boundary conditions.

1.2.2 Single Interface

Figure 1-4 shows a semi-infinite metal with negative real part of dielectric constant ε_1 interfaced with another semi-infinite dielectric with a positive real dielectric constant ε_2.

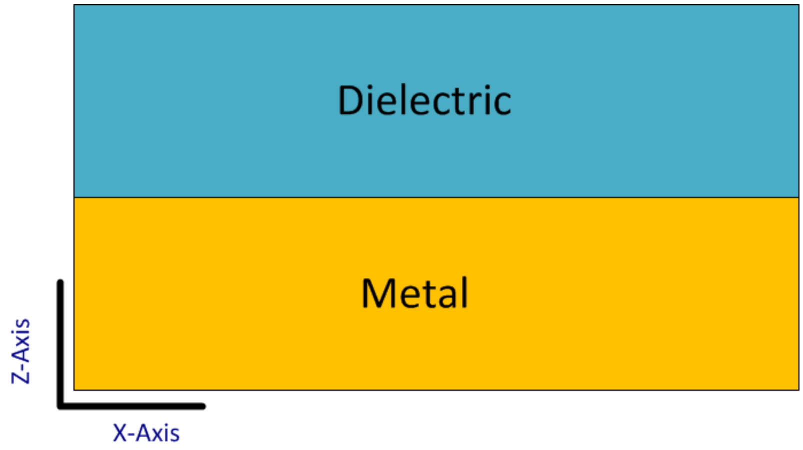

Figure 1-4 Single Interface between metal and dielectric.

The set of equations derived above must be solved in different regions using appropriate boundary conditions. Applying the boundary conditions to the TE polarization equations in both the regions, we get for $z > 0$, as

$$E_y(z) = A_2 e^{j\beta x} e^{-k_2 z} \tag{1.37}$$

$$H_x(z) = -jA_2 \frac{1}{\omega\mu_o} k_2 e^{j\beta x}\, e^{-k_2 z} \tag{1.38}$$

$$H_z(z) = -A_2 \frac{\beta}{\omega\mu_o} e^{j\beta x} e^{-k_2 z} \tag{1.39}$$

and for z<0, as

$$E_y(z) = A_1 e^{j\beta x} e^{k_2 z} \tag{1.40}$$

$$H_x(z) = jA_1 \frac{1}{\omega\mu_o} k_2 e^{j\beta x}\, e^{k_1 z} \tag{1.41}$$

$$H_z(z) = A_1 \frac{\beta}{\omega\mu_o} e^{j\beta x} e^{k_1 z} \tag{1.42}$$

The continuity conditions of H_x and E_y on the interface $(z = 0)$ when applied to equations 1.37, 1.38, 1.40 and 1.41 require

$$A_1(k_1 + k_2) = 0 \qquad 1.43$$

For a propagating mode confined to the surface it is essential that the real parts of k_1 and k_2 be positive. But for the above equation to satisfy the only possibility is $A_1 = 0$, which implies that the surface modes don't exist for TE polarization.

Now applying the boundary conditions to equation (1.34-1.36) for TM polarization we get the field equations.

The field equations for $z > 0$ is given by

$$H_y(z) = A_2 e^{j\beta x} e^{-k_2 z} \qquad 1.44$$

$$E_x(z) = jA_2 \frac{1}{\omega\varepsilon} k_2 e^{j\beta x} e^{-k_2 z} \qquad 1.45$$

$$E_z(z) = -A_1 \frac{\beta}{\omega\varepsilon_o\varepsilon_2} e^{j\beta x} e^{-k_2 z} \qquad 1.46$$

and for $z < 0$ as

$$H_y(z) = A_1 e^{j\beta x} e^{k_1 z} \qquad 1.47$$

$$E_x(z) = -jA_1 \frac{1}{\omega\varepsilon_o\varepsilon_1} k_2 e^{j\beta x} e^{k_1 z} \qquad 1.48$$

$$E_z(z) = -A_1 \frac{\beta}{\omega\varepsilon_o\varepsilon_1} e^{j\beta x} e^{k_1 z} \qquad 1.49$$

The continuity of H_y and E_z at the interface leads to the condition $A_1 = A_2$.

$$\frac{k_2}{k_1} + \frac{\varepsilon_2}{\varepsilon_1} = 0 \qquad 1.50$$

It is seen here that the surface modes exist for TM polarization at the interface of the metal and dielectric interface with opposite sign of their real dielectric permittivities, then the relation between the wave vector, propagation constant and dielectric constant can be written as

$$k_1^2\varepsilon = \beta^2 - k_o^2\varepsilon_1 \qquad 1.51$$

$$k_2^2\varepsilon = \beta^2 - k_o^2\varepsilon_2 \qquad 1.52$$

The propagation constant for the surface mode can be derived using equations 1.50-1.52 and is given by

$$\beta = k_o\sqrt{\frac{\varepsilon_1\varepsilon_2}{\varepsilon_1+\varepsilon_2}} \qquad 1.53$$

1.2.3 Multi-Layer Interface

Another configuration which can support surface plasmon is a multi-interface configuration containing alternating metal and dielectric layers. Surface plasmons are created on each interface and then these surface plasmons interact to give coupled modes. Figure 1-5 shows the multilayer configuration. There are two configurations possible from the geometry shown in the figure; Insulator-Metal–Insulator (IMI) and the other configuration is Metal-Insulator-Metal (MIM).

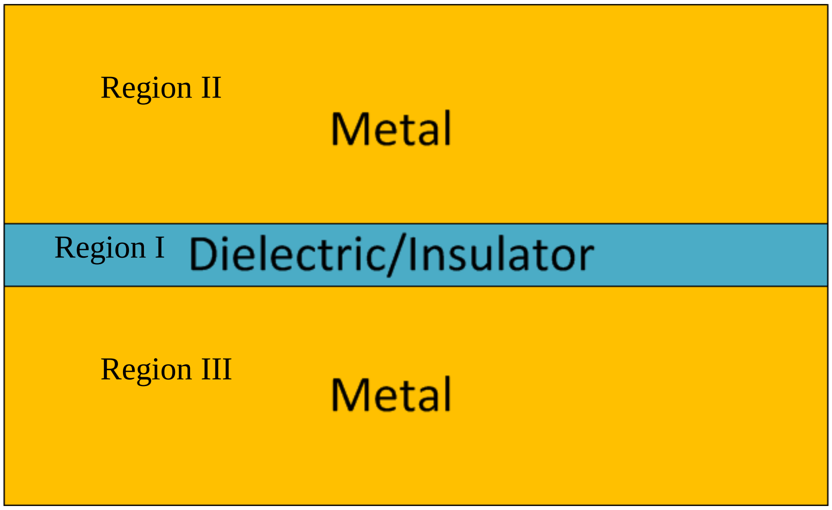

Figure 1-5 Multilayer configuration.

The field equations and the dispersion relations of the MIM configuration can be derived here by applying the boundary conditions.

for $z > a$ the field equations are given by,

$$H_y = A_1\, e^{j\beta x} e^{-k_3 z} \quad 1.54$$

$$E_x = jA_1 \frac{1}{\omega\varepsilon} k_3 e^{j\beta x} e^{-k_3 z} \quad 1.55$$

$$E_z = -A_1 \frac{\beta}{\omega\varepsilon_o\varepsilon_3} e^{j\beta x} e^{-k_3 z} \quad 1.56$$

and for $z < -a$ by

$$H_y = A_2 e^{j\beta x} e^{k_2 z} \quad 1.57$$

$$E_x = jA_2 \frac{1}{\omega\varepsilon} k_3 e^{j\beta x} e^{k_2 z} \quad 1.58$$

$$E_z = -A_3 \frac{\beta}{\omega\varepsilon_o\varepsilon_3} e^{j\beta x} e^{k_2 z} \quad 1.59$$

where $k_i = k_{1,2}$ are the wave-vector perpendicular to the interface. It is also seen that the fields decay exponentially in the claddings (region II) and (region III).

For the core region$-a < z < a$, the modes which exist on the bottom and top of the interface couple, to yield

$$H_y = A_3 e^{i\beta x} e^{k_1 z} + A_4 e^{i\beta x} e^{-k_1 z} \tag{1.60}$$

$$E_x = -iA_3 \frac{1}{\omega\varepsilon_o\varepsilon_1} k_1 e^{i\beta x} e^{k_1 z} + iA_4 \frac{1}{\omega\varepsilon_o\varepsilon_1} k_1 e^{i\beta x} e^{-k_1 z} \tag{1.61}$$

$$E_z = A_3 \frac{\beta}{\omega\varepsilon_o\varepsilon_1} e^{i\beta x} e^{ik_1 z} + A_4 \frac{\beta}{\omega\varepsilon_o\varepsilon_1} e^{i\beta x} e^{-k_1 z} \tag{1.62}$$

By applying the continuity condition for H_y and E_x on the two interfaces and the following condition

$$k_i^2 = \beta^2 - k_o^2 \varepsilon_i \tag{1.63}$$

where $i = 1,2,3$, the dispersion relation of the MIM configuration is obtained as

$$\tanh k_1 a = \frac{-k_2\varepsilon_1}{k_1\varepsilon_2} \tag{1.64}$$

$$\tanh k_1 a = \frac{-k_1\varepsilon_2}{k_2\varepsilon_1} \tag{1.65}$$

Equation 1.64 describes the odd vector parity for E_x and even for H_y and E_z, while equation 1.65 describes even vector parity for E_x and odd for H_y and E_z fields. This thesis uses the even parity mode for H_y.

1.3 Analysis of Localized Surface Plasmon Sensing

Localized surface plasmons are non-propagating oscillations of the conduction electrons of metallic nanostructures coupled to electromagnetic field. These oscillations are fundamental modes of the particle. These modes can be derived from the scattering problem solution of Maxwell’s equations of small, sub-wavelength conductive particle under the influence of an oscillating electromagnetic wave.

The oscillating electrons driven by the oscillating electromagnetic field are confined by the curved surfaces of the nanoparticles, and these curved surfaces exert an effective restoring force on these electrons. This leads to the electric field near the particle being enhanced, with maximum being on the surface and decreasing exponentially with distance from the surface as shown in Figure 1-6(a).

When at resonance, the particle’s optical *extinction* is highest and the nano particle acts like a resonator. This resonance wavelength is a mode of oscillation of the free electrons in the metal nano-particle Figure 1-6(a)

The resonant frequency is dependent on the plasmon frequency of the metal and also on the size, shape and the environment that surrounds the nano-particle Figure 1-6(b). This environment can also include other nano-particles in the close proximity and also refractive index of the medium in which the particles are placed. For noble metals like *silver* (Ag) and *gold* (Au) the resonance wavelength lies in the optical range.

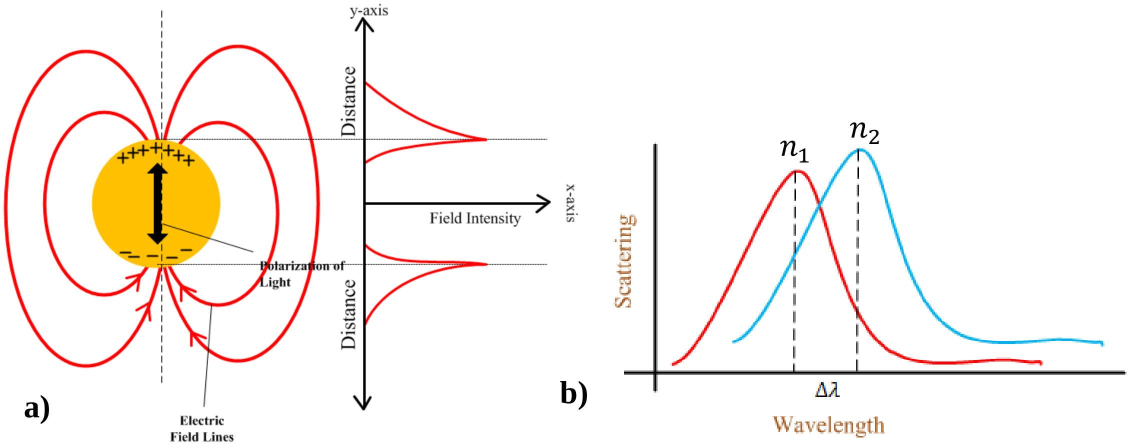

Figure 1-6 a) Field lines around a metal nano-particles and intensity b) Response of the particle at varying refractive index n_1 and n_2.

This thesis considers *silver* as the metal for nano-particles. Another advantage that nano-particles have is that exciting surface plasmons does not require elaborate arrangements for exciting propagating surface plasmons; direct shining of light is enough to excite plasmons.

Historically, this effect has found applications for staining glass used in windows and ornamental cups [7] albeit without understanding the underlying phenomenon. It was not until Gustav Mie [8] who described the scattering properties of nano-particles that gave a clear understanding of the resonating properties of metal nano-particles. To describe the properties of these nanoparticle resonators and their response to light, the scattering properties of these particles need to be studied. This was first described by Gustav Mie for spherical particles for diameters smaller than the wavelength of light ($d \ll \lambda$) [8] and given by the following equations

$$\sigma_{sca} = \frac{2\pi}{|k|^2}\sum_{L=1}^{\infty}(2L+1)(|a_L|^2 + |b_L|^2) \qquad 1.66$$

$$\sigma_{ext} = \frac{2\pi}{|k|^2}\sum_{L=1}^{\infty}(2L+1)[Re(a_L + b_L)] \qquad 1.67$$

$$\sigma_{abs} = \sigma_{ext} - \sigma_{sca} \qquad 1.68$$

where k is the incoming wave vector and L is an integer representing the resonating dipole, quadro-pole and higher multi-poles and a_L and b_L are composed of Ricatti-Bessel functions.

Mie theory and other closed form methods have been used to find solutions for simple and symmetrical nano-particles like nano-shells [9] and nano-ellipsoids [10].

When two or more nano-particle resonators are used in proximity they are coupled and give a different response than the single nano-particle. There is a huge enhancement in the intensity of the electric field on the axis joining the particles at resonant wavelengths. This can be used for giant enhancements of Raman spectrum signals and infrared spectroscopic signals of the order of $10^{14} - 10^{15}$ times. When these coupled nano-particles (resonators) are asymmetric in shape they give rise to fano resonances whose line-shape of resonance is extremely sensitive to the dielectric constant of the surrounding material [11][12]. When the dielectric constant of the surrounding material is changed there is a change in the peak resonance although the shape of the spectrum remains more or less the same. These measurements are generally done by measuring the extinction spectrum of the sensor, either experimentally or by simulation/calculation.

With such high enhancements in the intensity of the field, analytes with picomolar $(10^{-15}M)$ concentrations can also be analyzed and can be potentially used in detection of toxic chemicals or trace impurities dissolved in potable water.

Plasmonics aims to provide sensing using properties of electromagnetic waves, by measuring the changes in the refractive index of the material or by enhancing the already emitted electromagnetic wave from a molecule.

1.4 Sensing Parameters

Many parameters and features define the performance of SPR sensor: (1) sensor sensitivity (2) figure of merit (FOM) and (3) sensor resolution/Limit of detection. Sensor sensitivity is defined as the change in the measured signal corresponding to the change in the analytes concentration. The measured signal can be intensity, phase or spectral extinction peak position. Additional signals that can be measured for an SPR sensor can be angle of incidence and polarization of the incident wave interacting with the surface plasmons.

For different types of analytes the sensitivity measurements can be classified into two types, bulk refractive index sensing and surface sensing. In bulk refractive index sensitivity, the changes in refractive index units (RIU) of the bulk background (n_B) with measured signal change (δP) are calculated as

$$m_B = \frac{\delta P}{\delta n_B} \qquad 1.69$$

Surface sensing is used for bio-molecular interaction analysis i.e. to measure dielectric binding. Here, the changes in the effective thickness of the surface are measured in comparison to the changes in the signals. Thickness is measured assuming that the mass density of the biomolecules are proportional to effective thickness (d_S) and surface refractive index (n_s)

$$m_S = \frac{\delta P}{\delta d_s} \tag{1.70}$$

Another parameter that can measure the inherent difference between the various metal nano-structures and sensors is the figure of merit (FOM) defined as [13].

$$FOM = \frac{m(\text{eV } RIU^{-1})}{\Gamma(\text{eV})} \tag{1.71}$$

where m =sensitivity and $\Gamma =$ Full wave half maximum(FWHM) of the signal.

This quantity represents the ratio of sensitivity to line-width of the extinction peak for a particular structure. The larger the value of FoM the better the structure is for sensing. The figure of merit can be used for bulk sensing or surface sensing with the sensitivity term being m_B or m_S respectively.

Limit of detection (LOD) is the minimum change of the analyte concentration that can be detected. In any sensor, if the minimum detectable change of signal is given by σ and the sensitivity is m the limit of detection is given by

$$LOD = \frac{\sigma}{m} \tag{1.72}$$

This is an important parameter that describes the overall performance of the entire sensor equipment. LOD is affected by a number of factors like system noise, quality of surface chemistry and the receptor-analyte binding affinity. LOD cannot be used for direct comparison of different nanoparticles. For example, a poorly sensitive nanoparticle can have better LOD than a highly sensitive one, provided it has lower SNR.

1.5 Literature Review

Surface plasmons associated with metal particles have been historically used as colorants as seen in stained glass and ornamental cups (e.g. Lycagarus Cup) [7] though without understanding the underlying phenomenon. It was not until the late 19th century work done by Rayleigh, Mie and Gans that gave insight into how metal nanoparticles scatter light. Also, electron energy loss experiments on metal films confirmed the presence of surface plasmons [1]. Surface plasmons can be broadly classified as plasmons excited on metal film and dielectric interface and localized surface plasmons excited in metal nano-particles. Plasmonic bio-sensors can also be broadly divided into two categories, depending on the type of plasmon being used for sensing either Surface Plasmon Resonance (SPR) excited on simple metal-dielectric interface or a Localized Surface Plasmon Resonance (LSPR) involving particular shapes of metal nano-particles. The SPR sensors are basically thin film metals which detect the refractive index changes that occur near the metal film which carry surface plasmons. LSPR on nanoparticles on the other hand when used for label-free assays localizes the sensing volume and thereby reduces the amount of analyte needed to generate a signal.

Various research groups have thoroughly considered the optical properties of various geometric shapes and studied their sensing properties. Single and arrays of nano-shells and their variants have been studied for real time binding event analysis, surface enhanced raman spectroscopy (SERS) and plasmon enhanced fluorescence [14]. Nano-rings [15], Nano crescent [16], Nano-cube [13], Nano stars [17] have also been studied and their sensitivity and FoM quantified. Reference [5] gives an excellent review of many nanostructures that have been investigated in literature (Table 1-1)

Table 1-1 Summary of nano-particle shapes and their refractive index sensitivity parameters (adapted from [5]).

Particle	**Type**	$\boldsymbol{\lambda_{peak}}$ **(nm)**	$\boldsymbol{\Delta\lambda}$ **(nm)**	**FoM** $(\boldsymbol{RIU^{-1}})$
Au nanorice	Ensemble	1600	801	1.3
Ag sphere	Single	520	160	2.2
Au crescent	Ensemble	1795	596	2.8
Ag triangle	Single	760	350	3.8
Au bi-pyramid	Ensemble	681	352	4.4
Ag cube-sub	single	430	118	5.4
Au star	single	770	665	5.4

Metal nano-shells as plasmonic resonators have been a subject of very detailed investigations in the context of sensing and spectroscopy. They have been analyzed analytically, numerically and experimentally for their properties. Reference [18] investigates the variation of the local field enhancement due to the size of dielectric core and its variation in enhancement is measured using SERS. Reference [19] uses an array of nano-shells and combine surface vibrational spectroscopies (SERS and SEIRS) on a single substrate.

Various phenomena which are optical analogues have also been studied for use in bio-sensing like fano-resonance [20]. Reference [11] investigates fano resonances using symmetry breaking nanostructures acting as resonators and investigates its sensitivity, which was found to be 541 nm/RIU with a FoM of 8.34 RIU^{-1}. Reference [21] has used M-I-M waveguides and resonators to generate Fano resonance and its sensitivity to refractive index was found to be 900 nm/RIU with a FoM of 500 RIU^{-1}. Plasmonic nano-antennas [22][23][24] have also been used as sensors. Plasmonic ring structures have been a subject of extensive investigation [25] and other variations of it like split ring resonators [26][27], complementary split ring resonators have also been investigated [28] and used for sensing [29][30][15]. The sensitivities have been found to range from 480 nm/RIU to 880 nm/RIU with FoM varying from 1.3 RIU^{-1} to 2 RIU^{-1}.

Among other structures, Metal-Insulator-Metal waveguide is one such structure which has also been studied extensively due to its property of being immune to diffraction limit of light and allowing sub-wavelength confinement and guiding of light at nano-scale. Plasmonic waveguides have attributes of strong confinement [31] and extremely low bending loss [32]. Various structures of the M-I-M configuration have been tested and reported in literature like resonators [33]-[34] directional couplers [35] and filters [36].

Emitters coupled to metal particles or thin metal films have been studied in literature [37][38][39]. There is a huge increase in enhancement of the near-field intensity due to interference. Also, there is a change in the local density of states [24] and change (increase) in the decay-rate of the emitter (Purcell effect) thus controlling the radiative properties of emitters [40][41]. These properties of plasmon coupled emitters have also been tested numerically using FDTD [42] or Green's Dyadic functions [37]. All these have been used in control of light for design of nano lasers [43]. Though this effect has been suggested for bio-sensing but never been tested using multiple sensitivities using large near field enhancement and also the emission properties of the emitters.

In any of the reports mentioned above, computational methods of electromagnetic theory are extremely essential either to predict a certain behavior or to confirm certain experimental observation. The Finite Difference Time Domain (FDTD) method is a popular computational tool for the solution of Maxwell’s equations [44]. Its popularity stems from the fact that it has explicit time marching capability, simplicity and it directly gives the field values. References [45] and [46] have used FDTD to investigate the optical properties and local field enhancement of nano-shell dimers and nano-shells for use in SERS.

1.6 Thesis Objectives

The main contribution of this work is the incorporation of multiple sensitivities in the design of bio sensors using nano-plasmonic structures. The proposed passive design utilizes the sensitivity of MIM structures together with the ring-resonator, whereas the active structure design utilizes the sensitivity of the plasmonic nanoparticles' resonances to the surroundings combined with the emitter sensitivity.

The specific objectives are as follows

1. To conduct an extensive literature survey on different types of structures and phenomenon associated with surface plasmons used in bio-sensing.
2. Build a 2D-EM simulator that accounts for properties of the plasmonic structures and active material utilizing the Auxiliary Differential Equation-FDTD technique.
3. Numerically analyze the propagation of passive biosensors based on plasmonic ring resonators.
4. Numerically analyze the sensing properties of specific active plasmonic structures.
5. Extract important conclusions regarding the above design strategies.

1.7 Thesis Organization

This Thesis investigates the use of various plasmonic resonators in bio-sensing

- Chapter 1 discussed the basic theory of Surface plasmons which can be excited on planar interfaces and also on nano-particles. This chapter discusses bio-sensing and various parameters that would be measured during the thesis.
- Chapter 2 discusses Finite Difference Time-Domain algorithm using the Yee’s mesh, various material models that are available in literature. This thesis also discusses the General ADE FDTD algorithm and tools like Perfectly Matched Layer (PML) and Total Field Scattered Field (TFSF) boundary conditions that are integral to this thesis.
- Chapter 3 discusses MIM ring resonator and MIM ring based resonator Verification of the device using the dispersion relation is done. This chapter investigates the sensing properties of these devices.
- Chapter 4 discusses the nanoparticle based resonator and verifies the scattering properties of the particles using their dispersion relation. This chapter optimizes the nano-particle structure to a particular emission wavelength and uses it for sensing.
- Chapter 5 contains the summary of the thesis, future work and potential extensions.

Chapter 2

TIME DOMAIN SIMULATION ALGORITHM

The Finite Difference Time Domain method is a well-developed and a popular technique for the solution of Maxwell's equation. In this chapter, the details of the time domain algorithm using Yee's mesh as well as the incorporation of various material models into FDTD using General ADE FDTD algorithm are discussed. Also, tools that complement the FDTD solution like material independent Perfectly Matched Layer (MI-PML) and Total Field/Scattered Field (TF/SF) boundary conditions will also be discussed in detail.

2.1 Finite Difference Time Domain Method

The Finite-Difference Time Domain (FDTD) method is a brute force numerical algorithm which solves the Maxwell's equations using the Yee's mesh. This algorithm was first proposed by Yee in 1966 [44]. In the early days, FDTD was not well received. It was computationally 'heavy' due to problems with the absorbing boundary conditions. It was not until Mur developed an efficient absorbing boundary condition [47] in 1981 that research involving usage of FDTD saw an exponential increase [48]. It became all the more popular after the development of the Perfectly Matched Layer (PML) absorbing boundary condition [49].

FDTD has come a long way and has become the most popular algorithm for the solution of Maxwell's equations for research in photonics and its allied fields.

A lot of research has gone into the development of FDTD to make it more reliable and reduce the cost of computation. A method to find the far-field characteristics of scatterer was developed called as the Total-Field/Scattered Field (TF/SF) boundary condition [50].

FDTD has a problem with the mesh size - finer the mesh higher is the computational cost – so to overcome that problem non-uniform gridding was developed so as to have a fine mesh where the structure is located and coarse elsewhere. This partially reduced the computational cost without affecting the quality of results [49]. FDTD was also implemented for parallel computation using Open MPI, this reference [51] gives an excellent review in that direction.

Militaristic goals drove the initial adoption of FDTD. It was used in developing radar technologies, High-power microwave (HPM) beams and electromagnetic pulse protection to name a few. Now FDTD is used to design technologies in cell-phones, computers, lasers, to model quantum-mechanical effects, biological sensors and photonics.

2.1.1 FDTD solution of Maxwell's equation

Consider a non-dispersive, linear, isotropic and source-free formulation of the equations 1.6 and 1.7, as

$$\frac{\partial \mathrm{H}}{\partial t} = -\frac{1}{\mu}\nabla \times \mathrm{E} \qquad 2.1$$

$$\frac{\partial \mathrm{E}}{\partial t} = \frac{1}{\varepsilon}\nabla \times \mathrm{H} \qquad 2.2$$

Expanding the above equations into its components and expressing in scalar form would give the following six coupled equations

$$\frac{\partial E_z}{\partial y} - \frac{\partial E_y}{\partial z} = -\frac{\partial H_x}{\partial t} \tag{2.3}$$

$$\frac{\partial E_x}{\partial z} - \frac{\partial E_z}{\partial x} = -\frac{\partial H_y}{\partial t} \tag{2.4}$$

$$\frac{\partial E_y}{\partial x} - \frac{\partial E_x}{\partial y} = -\frac{\partial H_z}{\partial t} \tag{2.5}$$

$$\frac{\partial H_z}{\partial y} - \frac{\partial H_y}{\partial z} = \frac{\partial E_x}{\partial t} \tag{2.6}$$

$$\frac{\partial H_x}{\partial z} - \frac{\partial H_z}{\partial x} = \frac{\partial E_y}{\partial t} \tag{2.7}$$

$$\frac{\partial H_y}{\partial x} - \frac{\partial H_x}{\partial y} = \frac{\partial E_z}{\partial t} \tag{2.8}$$

The generalized FDTD algorithm using Yee's mesh discretizes the above differential equations in both time and space using the central difference approximation for first order partial derivatives.

2.1.2 Yee's Mesh

Yee's orthogonal mesh has both the electric field (E) and magnetic field (H) components staggered in time and space. As illustrated in Figure 2-1 E and H are off-set in space such that every H component is surrounded by four E components. This scheme allows central differences to be used without any inconsistency making the algorithm second order accurate. For the same reason E and H are also off-set in time, at time step $n + 1/2$ the electric field is calculated and at time step $n + 1$ magnetic field is calculated.

This arrangement in space also gives a very intuitive arrangement of the fields linking them to the Ampere's law and Faraday's law.

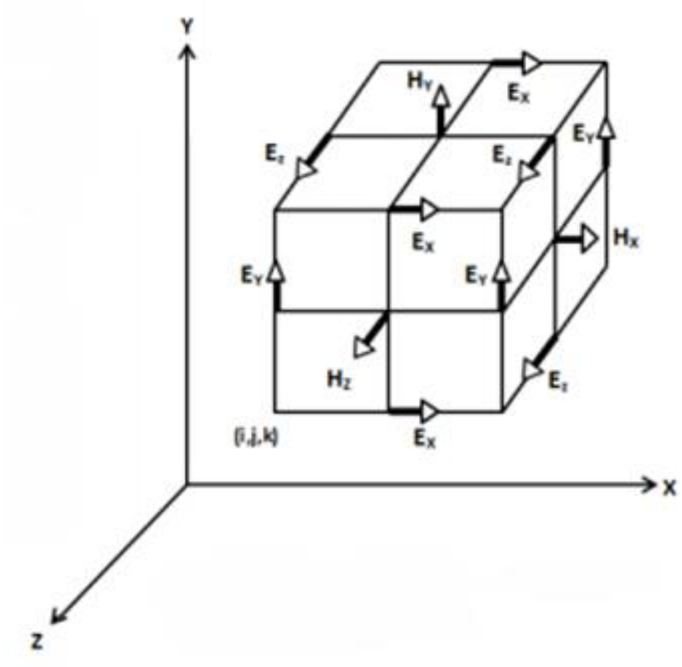

Figure 2-1 Yee's Mesh (adapted from [52])

In this thesis, a 2-dimensional space on the x-y plane and no variation of fields along the z-axis is assumed. This implies that

$$\frac{\partial H_y}{\partial z} = 0, \frac{\partial H_x}{\partial z} = 0, \frac{\partial E_y}{\partial z} = 0, \frac{\partial E_x}{\partial z} = 0 \qquad 2.9$$

The set of equations 2.1- 2.8 for TM polarized fields simplify to,

$$\frac{\partial E_x}{\partial t} = \frac{1}{\varepsilon}\,\frac{\partial H_z}{\partial y} \qquad 2.10$$

$$\frac{\partial E_y}{\partial t} = -\frac{1}{\varepsilon}\,\frac{\partial H_z}{\partial x} \qquad 2.11$$

$$\frac{\partial H_z}{\partial t} = \frac{1}{\mu}\left(\frac{\partial E_x}{\partial y} - \frac{\partial E_x}{\partial y}\right) \qquad 2.12$$

and for TE polarized fields it simplifies to

$$\frac{\partial H_x}{\partial t} = -\frac{1}{\mu}\frac{\partial E_z}{\partial y} \tag{2.13}$$

$$\frac{\partial H_y}{\partial t} = \frac{1}{\mu}\frac{\partial E_z}{\partial x} \tag{2.14}$$

$$\frac{\partial E_z}{\partial t} = \frac{1}{\varepsilon}\left(\frac{\partial H_y}{\partial x} - \frac{\partial H_x}{\partial y}\right) \tag{2.15}$$

As it was seen previously surface plasmons are excited only using TM polarization. The TM polarized 2-dimensional equations (2.10- 2.12) are discretized first in space then in time as shown below.

$$\frac{\partial E_x}{\partial t} = \frac{1}{\varepsilon}\,\frac{\big(H_z(i,j) - H_z(i,j-1)\big)}{\Delta y} \tag{2.16}$$

$$\frac{\partial E_y}{\partial t} = -\frac{1}{\varepsilon}\,\frac{\big(H_z(i,j) - H_z(i-1,j)\big)}{\Delta x} \tag{2.17}$$

$$\frac{\partial H_z}{\partial t} = \frac{1}{\mu}\left(\frac{\big(E_x(i,j+1) - E_x(i,j)\big)}{\Delta y} - \frac{\big(E_y(i+1,j) - E_y(i,j)\big)}{\Delta x}\right) \tag{2.18}$$

For the central difference to be found in time for equation (2.16- 2.18) Yee's mesh is assumed where E and H are off-set by $1/2$ time step as seen in Figure 2-2

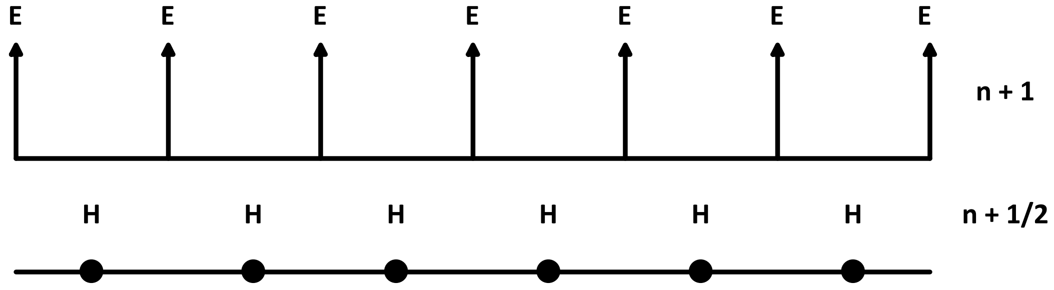

Figure 2-2 Time domain representation of the Yee's algorithm.

$$\frac{E_x^{n+1}\left(i+\frac{1}{2},j\right)-E_x^{n}\left(i+\frac{1}{2},j\right)}{\Delta t} = -\frac{1}{\varepsilon}\,\frac{H_z^{n+\frac{1}{2}}\left(i+\frac{1}{2},j+\frac{1}{2}\right)-H_z^{n+\frac{1}{2}}\left(i+\frac{1}{2},j-\frac{1}{2}\right)}{\Delta y} \qquad 2.19$$

$$\frac{E_y^{n+1}\left(i,j+\frac{1}{2}\right)-E_y^{n}\left(i,j+\frac{1}{2}\right)}{\Delta t} = -\frac{1}{\varepsilon}\,\frac{H_z^{n+\frac{1}{2}}\left(i+\frac{1}{2},j+\frac{1}{2}\right)-H_z^{n+\frac{1}{2}}\left(i-\frac{1}{2},j+\frac{1}{2}\right)}{\Delta x} \qquad 2.20$$

$$\frac{H_z^{n+\frac{1}{2}}\left(i+\frac{1}{2},j+\frac{1}{2}\right)-H_z^{n-\frac{1}{2}}\left(i+\frac{1}{2},j+\frac{1}{2}\right)}{\Delta t} = \frac{1}{\mu}\left(\frac{E_x^{n}\left(i+\frac{1}{2},j+1\right)-E_x^{n}\left(i+\frac{1}{2},j\right)}{\Delta y} - \frac{E_y^{n}\left(i+1,j+\frac{1}{2}\right)-E_y^{n}\left(i,j+\frac{1}{2}\right)}{\Delta x}\right) \qquad 2.21$$

The above equations are now discretized in both time and space using the Yee's mesh. For the stability of the discretization in time an upper limit on the time step Δt is found using the Courant stability condition which is found using the spatial cell size i.e $\Delta x, \Delta y$ and Δz. This stability condition is given for a three dimensional case by

$$\Delta t \leq \Delta t_{max} = \frac{1}{c\sqrt{\left(\frac{1}{\Delta x^2}+\frac{1}{\Delta y^2}+\frac{1}{\Delta z^2}\right)}} \qquad 2.22$$

where $c =$ velocity of light in the medium and for 2-dimensional case Δz is ignored. This is the only stability condition required for FDTD. The choice of the spatial cell size depends on the problem that is being solved. For photonic applications the size is taken to be around $\lambda/100$, where λ is the smallest wavelength which is being used in the problem.

2.2 Material Models

When a material is considered to be dispersive then its behavior can be described by the following constitutive relations in the frequency domain.

$$D(\omega) = \varepsilon(\omega)E(\omega) \qquad 2.23$$

$$P(\omega) = \varepsilon_o \chi(\omega) E(\omega) \qquad 2.24$$

Where $P(\omega)$ -the frequency dependent polarization- is induced in the material due to an external electric field $E(\omega)$ and χ is the susceptibility of the medium, which measures the ability of the dielectric to polarize in an applied dielectric field. Using equations (2.23-2.24) it can be written as

$$D(\omega) = \varepsilon_o E(\omega)\big(1 + \chi(\omega)\big) \qquad 2.25$$

and also the permittivity can be written as

$$\varepsilon(\omega) = \varepsilon_o\big(1 + \chi(\omega)\big) \qquad 2.26$$

with relative permittivity as

$$\varepsilon_r(\omega) = 1 + \chi(\omega) \qquad 2.27$$

With the above expression it is now possible to assign a material model depending on the properties of the material. The models would be fore with discussed and used later deal with macroscopic polarization and are based on classical electron oscillator (CEO).

2.2.1 The Drude Model

Drude model is based on the assumption that a sea of electrons inside the bulk of the material are free and constantly in motion bouncing off heavier immobile and relatively heavier ions. These electrons when placed in an electric field align themselves along the field. This motion is dampened by electrons collisions with the ions and there is no interaction between the electrons themselves. Using Newton’s Laws of motion the relation between polarization and electric field is found to be

$$P(\omega) = \frac{ne^2}{m(j\Gamma\omega - \omega^2)} E(\omega) \qquad 2.28$$

where $m =$ mass of the electron, $\Gamma =$ damping constant, $n =$ electron density and e =charge of the electron, using equation 2.24 susceptibility can be found as

$$\chi(\omega) = \frac{P(\omega)}{\varepsilon_o E(\omega)} = \frac{ne^2}{m(j\Gamma\omega - \omega^2)} \qquad 2.29$$

Using equation 2.26 the relative permittivity can be written as

$$\varepsilon_r(\omega) = 1 + \frac{ne^2}{m(j\Gamma\omega - \omega^2)} = 1 + \frac{\omega^2{}_p}{j\Gamma\omega - \omega^2} \qquad 2.30$$

where ω_p =plasma frequency which is a constant for particular metal.

2.2.2 The Lorentz Model

The Lorentz oscillator model takes into consideration the electrons that are bounded to the atoms. This model uses the analogy of a spring-mass system. If an electric field is applied the electron under the influence of the force would start oscillating like a mass bounded to a spring. The spring has a restoring force due to the nucleus. When laws of motion are applied to this system the relation between polarization and electric field is given by

$$P(\omega) = \frac{ne^2}{m(\omega_o^2 + j\Gamma\omega - \omega^2)} E(\omega) \qquad 2.31$$

Susceptibility is given by

$$\chi(\omega) = \frac{P(\omega)}{\varepsilon_o E(\omega)} = \frac{ne^2}{m(\omega_o^2 + j\Gamma\omega - \omega^2)} \qquad 2.32$$

2.2.3 The Lorentz Drude Model

Lorentz-Drude model is the most generalized model describing a metal under the influence of an electromagnetic field. This model incorporates two types of electrons in the metal both free and bound electrons. The permittivity is described by permittivity due to free electrons (Drude) and also due to the bounded electrons (Lorentz) as

$$\varepsilon = \varepsilon_{free} + \varepsilon_{bound} \tag{2.33}$$

$$\varepsilon_{free} = 1 + \frac{\omega_p^2}{j\Gamma\omega - \omega^2} \tag{2.34}$$

The permittivity characterized by bound electrons is described by

$$\varepsilon_{bound} = \frac{\omega_p^2}{\omega_o^2 + j\Gamma\omega - \omega^2} \tag{2.35}$$

where, ω_p is the plasma frequency

$$D(\omega) = \varepsilon_o\left(1 + \frac{\omega_p^2}{j\Gamma\omega - \omega^2} + \frac{\omega_p^2}{\omega_o^2 + j\Gamma\omega - \omega^2}\right) \tag{2.36}$$

The metal used in thesis is *silver* which is assumed to be dispersive and its permittivity is modeled using the Lorentz-Drude model Figure 2-3.

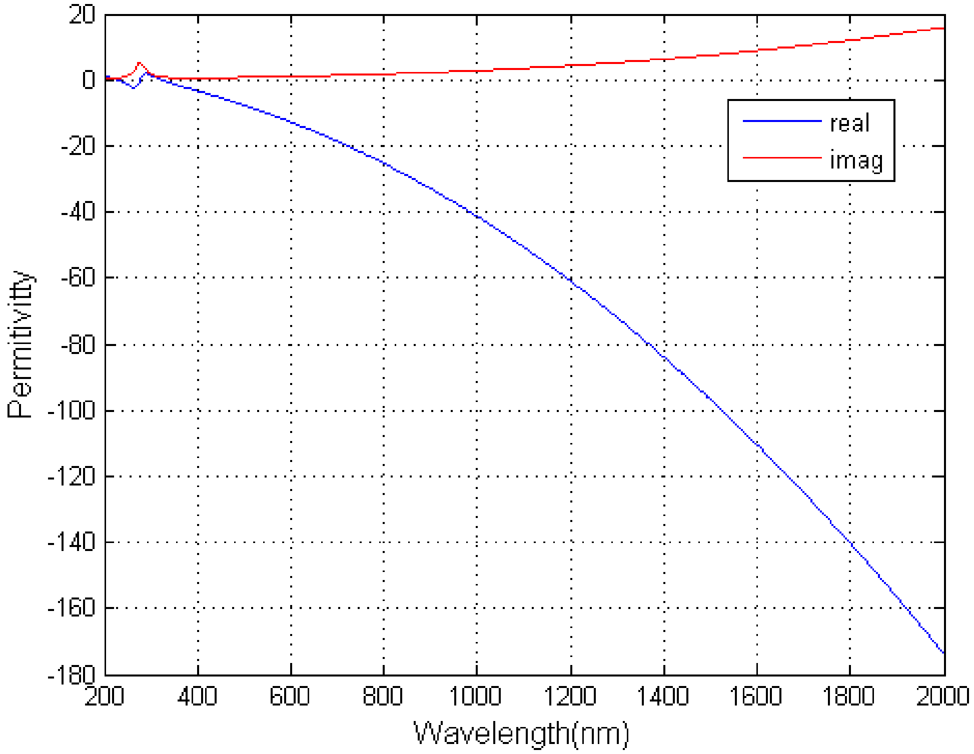

Figure 2-3 6-Pole Lorentz-Drude Model of Ag.

2.3 Auxiliary Differential Equation FDTD

Auxiliary Differential Equation formulation is a representation of the FDTD that takes into account a more general representation of the dispersion relation. This method converts the frequency dependent dispersion relation to time-domain using inverse Fourier transform. For example, for a Debye model type material the relation between D and E would be given by the following equations.

$$D(\omega) = \varepsilon_0 \frac{\sigma}{j\omega} E(\omega) \qquad 2.37$$

$$j\omega D(\omega) = \varepsilon_0 \sigma E(\omega) \qquad 2.38$$

when inverse Fourier transform is applied to equation 2.38 it becomes

$$\frac{\partial D(t)}{\partial t} = \varepsilon_0 \sigma E(t) \qquad 2.39$$

This can now be discretized using a forward difference scheme giving

$$\frac{D^{n+1} - D^{n}}{\Delta t} = \varepsilon_0 \sigma E^{n+1} \qquad 2.40$$

which can be rearranged to find the updated E given by

$$E^{n+1} = \frac{D^{n+1} - D^{n}}{\varepsilon_0 \sigma \Delta t} \qquad 2.41$$

The General ADE FDTD [53] goes further and includes the most general form of dispersion relation. This algorithm can include multi-pole Lorentz-Drude multi-pole model. This algorithm can be used to include any dispersion relation without any major change.

Before the value of E is calculated polarization is calculated using the dispersion relation of the material. Polarization is frequency dependent and needs to be converted to a time dependent expression which is done using the inverse Fourier transform. The procedure for finding the time-domain expression is as follows. Assume a single pole Lorentz model as given below

$$P(\omega) = \frac{a}{b + jc\omega - d\omega^{2}} E(\omega) \qquad 2.42$$

Applying inverse Fourier transform to equation 2.42 gives

$$bP(t) + cP'(t) + dP''(t) = aE(t) \tag{2.43}$$

This equation is discretized as

$$bP^n + c\frac{P^{n+1} - P^{n-1}}{2\Delta t} + d\frac{P^{n+1} - 2P^n + P^{n-1}}{\Delta t^2} = aE^n \tag{2.44}$$

Rearranging the terms in equation 2.44

$$P^{n+1} = \frac{4d - 2b\Delta t^2}{2d + c\Delta t}P^n + \frac{-2d + c\Delta t}{2d + c\Delta t}P^n + \frac{2a\Delta t^2}{2d + c\Delta t}E^n \tag{2.45}$$

This can be simplified and written as

$$P^{n+1} = C_1P^n + C_2P^{n-1} + C_3E^n \tag{2.46}$$

with $C_1 = \frac{4d-2b\Delta t^2}{2d+c\Delta t}, C_2 = \frac{-2d+c\Delta t}{2d+c\Delta t}, C_3 = \frac{2a\Delta t^2}{2d+c\Delta t}$

The above derivation is for a single pole dispersion relation but can be extended to multi pole models and here the multiple poles can be either from single material or different materials. For multiple poles the expressions are as follows

$$b_iP_i(t) + c_iP_i{}'(t) + d_iP_i{}''(t) = a_iE(t) \tag{2.47}$$

$$P_i{}^{n+1} = \frac{4d_i - 2b_i\Delta t^2}{2d_i + c_i\Delta t}P_i{}^n + \frac{-2d_i + c_i\Delta t}{2d_i + c_i\Delta t}P_i{}^{n-1} + \frac{2a_i\Delta t^2}{2d_i + c_i\Delta t}E^n \tag{2.48}$$

$$P_i^{n+1} = C_{1i}P_i^n + C_{2i}P_i^{n-1} + C_{3i}E^n \tag{2.49}$$

where $i = 1,2,3 \dots, N$

This thesis uses a 6-pole Lorentz Drude model for silver [54] . The calculation of electric field (E) is done as follows

$$D^{n+1} = \varepsilon_0 \varepsilon_\infty E^{n+1} + \sum_i^N P_i^{n+1} \tag{2.50}$$

$$E^{n+1} = \frac{(D^{n+1} - \sum_i^N P_i^{n+1})}{\varepsilon_0 \varepsilon_\infty} \tag{2.51}$$

With equation 2.51 giving the updated value of E.Figure 2-4 shows the flow-chart of the time loop of the general ADE algorithm

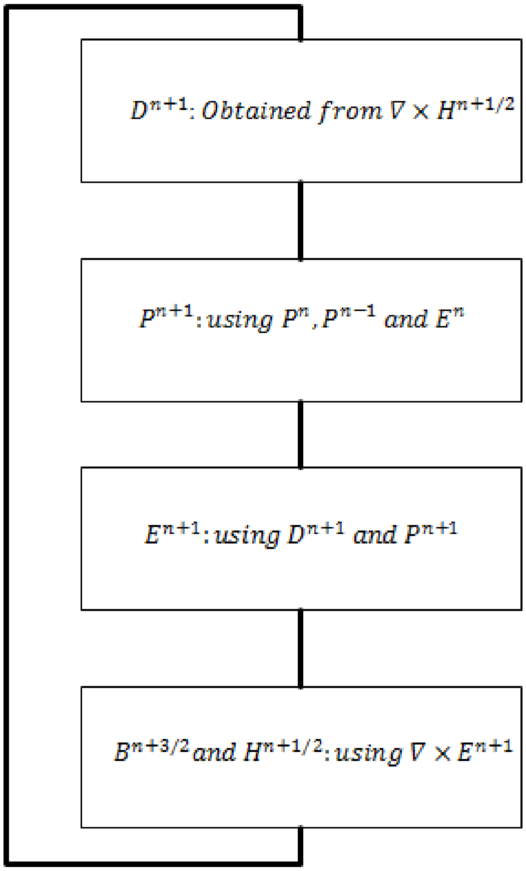

Figure 2-4 Flow Chart of the General ADE algorithm

2.4 Absorbing Boundary Condition

Perfectly Matched layer (PML) is an absorbing boundary condition developed by Berenger [55]. Berenger PML uses electric and magnetic conductivity values and also split H fields for a TM case. This thesis implements the Material Independent PML[56]

The magnetic and the electric conductivity so that there is no reflection is given by

$$\sigma_m = \sigma_e \qquad 2.52$$

where σ_e and σ_m are electrical and magnetic conductivities and calculated using

$$\sigma_{m,e}(\rho) = \sigma_{m,e(max)} \left(\frac{\rho}{\delta}\right)^n \qquad 2.53$$

and $\sigma_{m,e(max)} = -\frac{(n+1)c \log R_0}{2pml_n \Delta}$

2.5 Total Field/Scattered Field boundary conditions

The simulation region contains a total field and a scattered field region (TF/SF). These two regions are separated by a TF/SF boundary. The TF/SF is used to generate a high-quality plane wave using a two-grid formalism described in [49]. A pulse is simulated on an auxiliary 1-D grid at the source point and the rest is calculated using the normal FDTD update equations. The fields on the auxiliary 1-D are mapped into the two dimensional grid. These two grids must have same values of Δx and Δt. In the TF/SF formulation it is assumed that the field can be split in two components as shown below.

$$E_{total} = E_{inc} + E_{scat} \qquad H_{total} = H_{inc} + H_{scat} \qquad 2.54$$

TF/SF boundary condition divides the computational domain into two regions, as shown in Figure 2-5 Region-A and Region-B. The boundary is a non-physical virtual boundary which connects fields in these regions.

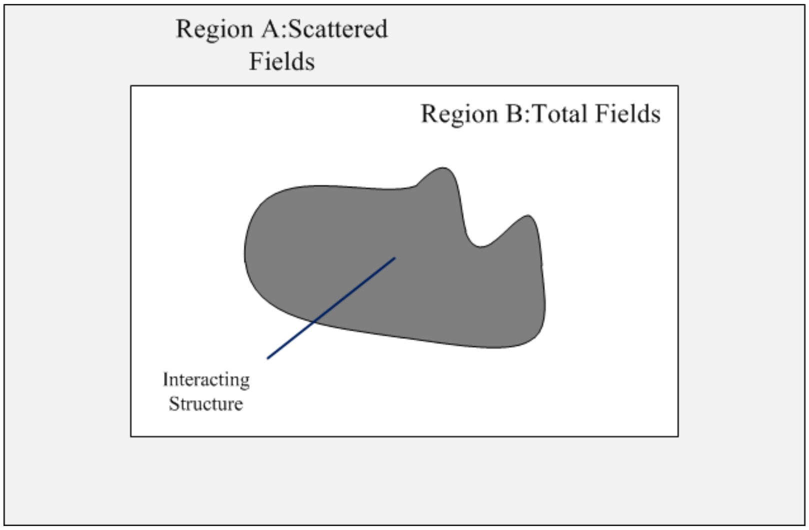

Figure 2-5 TFSF boundary conditions.

In Region-A Maxwell’s equations act on the total-field components, necessarily including both the incident and the scattered field component. In Region-B Maxwell’s equation act only on the scattered fields implying that there is no incident field in that region.

Yee’s algorithm is applied to the whole computational domain (Region-A and Region-B) but an inconsistency would arise at the boundary separating the two regions i.e. on the side of Region-A it is assumed that the fields calculated are scattered fields and on the side of the Region-B it is assumed that the fields calculated are total fields. This inconsistency can be removed by using equations (2.19 - 2.22) and equation -2.54 on the TF/SF boundary separating the two regions. Before applying the FDTD algorithm it is necessary to define the boundary and what fields are to be considered total and what fields to be considered scattered.

In Region B (Total-Field) the FDTD (in Figure 2-5) solution to for E_x would be

$$E_{x,total}^{n+1}\left(i+\frac{1}{2},j\right) = \tag{2.55}$$

$$E_{x,total}^{n}\left(i+\frac{1}{2},j\right)-\frac{\Delta\mathrm{t}}{\varepsilon\Delta\mathrm{y}}\left(H_{z,total}^{n+\frac{1}{2}}\left(i+\frac{1}{2},j+\frac{1}{2}\right)-H_{z,total}^{n+\frac{1}{2}}\left(i+\frac{1}{2},j-\frac{1}{2}\right)\right)$$

and correspondingly in Region A (Scattered Field) it would be

$$E_{x,scat}^{n+1}\left(i+\frac{1}{2},j\right) = \tag{2.56}$$

$$E_{x,scat}^{n}\left(i+\frac{1}{2},j\right)-\frac{\Delta\mathrm{t}}{\varepsilon\Delta\mathrm{y}}\left(H_{z,scat}^{n+\frac{1}{2}}\left(i+\frac{1}{2},j+\frac{1}{2}\right)-H_{z,scat}^{n+\frac{1}{2}}\left(i+\frac{1}{2},j-\frac{1}{2}\right)\right)$$

at the interface of the two regions solution would be (if taken on the bottom side of the interface)

$$E_{x,total}^{n+1}\left(i+\frac{1}{2},j_1\right) = \tag{2.57}$$

$$E_{x,total}^{n}\left(i+\frac{1}{2},j_1\right)-\frac{\Delta\mathrm{t}}{\varepsilon\Delta\mathrm{y}}\left(H_{z,total}^{n+\frac{1}{2}}\left(i+\frac{1}{2},j_1+\frac{1}{2}\right)-H_{z,scat}^{n+\frac{1}{2}}\left(i+\frac{1}{2},j_1-\frac{1}{2}\right)\right)$$

The inconsistency seen in the equation 2.57 can be removed by substituting equation 2.54 for H fields giving the equation

$$E_{x,total}^{n+1}\left(i+\frac{1}{2},j_1\right) = \tag{2.58}$$

$E_{x,total}^{n}\left(i+\frac{1}{2},j_1\right)-\frac{\Delta \mathrm{t}}{\varepsilon\Delta \mathrm{y}}\left(H_{z,total}^{n+\frac{1}{2}}\left(i+\frac{1}{2},j_1+\frac{1}{2}\right)-H_{z,total}^{n+\frac{1}{2}}\left(i+\frac{1}{2},j_1-\right.\right.$

$\left.\left.\frac{1}{2}\right)\right)+\frac{\Delta \mathrm{t}}{\varepsilon\Delta \mathrm{y}}H_{z,inc}^{n+1/2}\left(i+\frac{1}{2},j_1-\frac{1}{2}\right)$

which can be simplified to for $j=j_1$

$$E_{x,total}^{n+1}\left(i+\frac{1}{2},j_1\right)=E_{x,total}^{n+1}\left(i+\frac{1}{2},j_1\right)\ +\ \frac{\Delta \mathrm{t}}{\varepsilon\Delta \mathrm{y}}H_{z,inc}^{n+1/2}\left(i+\frac{1}{2},j_1-\frac{1}{2}\right) \quad 2.59$$

This is repeated for all the sides of the boundary, for $j=j_2$

$$E_{x,total}^{n+1}\left(i+\frac{1}{2},j_2\right)=E_{x,total}^{n+1}\left(i+\frac{1}{2},j_2\right)\ -\ \frac{\Delta \mathrm{t}}{\varepsilon\Delta \mathrm{y}}H_{z,inc}^{n+1/2}\left(i+\frac{1}{2},j_2+\frac{1}{2}\right) \quad 2.60$$

Similarly for E_y at $i=i_1$

$$E_{y,total}^{n+1}\left(i_1+1,j+\frac{1}{2}\right)=E_{x,total}^{n+1}\left(i_1+1,j+\frac{1}{2}\right)\ +\ \frac{\Delta \mathrm{t}}{\varepsilon\Delta \mathrm{y}}H_{z,inc}^{n+1/2}\left(i_1+\frac{1}{2},j-\frac{1}{2}\right) \quad 2.61$$

and at $i=i_2$

$$E_{y,total}^{n+1}\left(i_2+1,j+\frac{1}{2}\right)=E_{x,total}^{n+1}\left(i_2+1,j+\frac{1}{2}\right)\ -\ \frac{\Delta \mathrm{t}}{\varepsilon\Delta \mathrm{y}}H_{z,inc}^{n+1/2}\left(i_2+\frac{3}{2},j-\frac{1}{2}\right) \quad 2.62$$

A similar procedure is followed for the correction of H_z fields.

The calculation of $H_{z,inc}$, $E_{x,inc}$ and $E_{y,inc}$ is done using FDTD on Maxwell's equations in 1-D auxiliary computational domain as shown below

$$E_{1D,inc}^{n+1}(m)=\ E_{1D,inc}^{n}(m)+\frac{\Delta t}{\varepsilon\Delta x}\left(H_{1D,inc}^{n+\frac{1}{2}}(m-1/2)-H_{1D,inc}^{n+\frac{1}{2}}(m+1/2)\right) \quad 2.63$$

$$H_{1D,inc}^{n+1/2}(m+\frac{1}{2})=H_{1D,inc}^{n-\frac{1}{2}}(m+\frac{1}{2})+\frac{\Delta t}{\mu_o\Delta x}(E_{1D,inc}^{n}(m)-E_{1D,inc}^{n}(m+1)) \quad 2.64$$

$$H_{z,inc}^{n+1/2}(d) = H_{1D,inc}^{n+1/2}(d) \qquad 2.65$$

$$E_{x,inc}^{n+1}(d) = E_{1D,inc}^{n+1} cos\phi$$

$$E_{y,inc}^{n+1}(d) = -E_{1D,inc}^{n+1} sin\phi$$

where d is the representative location of the field and ϕ is the angle at which the incident plane wave is oriented at. Figure 2-6 shows a flow chart detailing how TFSF boundary condition is integrated in the General ADE FDTD algorithm. Figure 2-7 shows the computational window. Figure 2-8 and Figure 2-9 show the profile of the plane wave with and without a scatterer (circular perfect electric conductor) using a TFSF and PML boundary conditions.

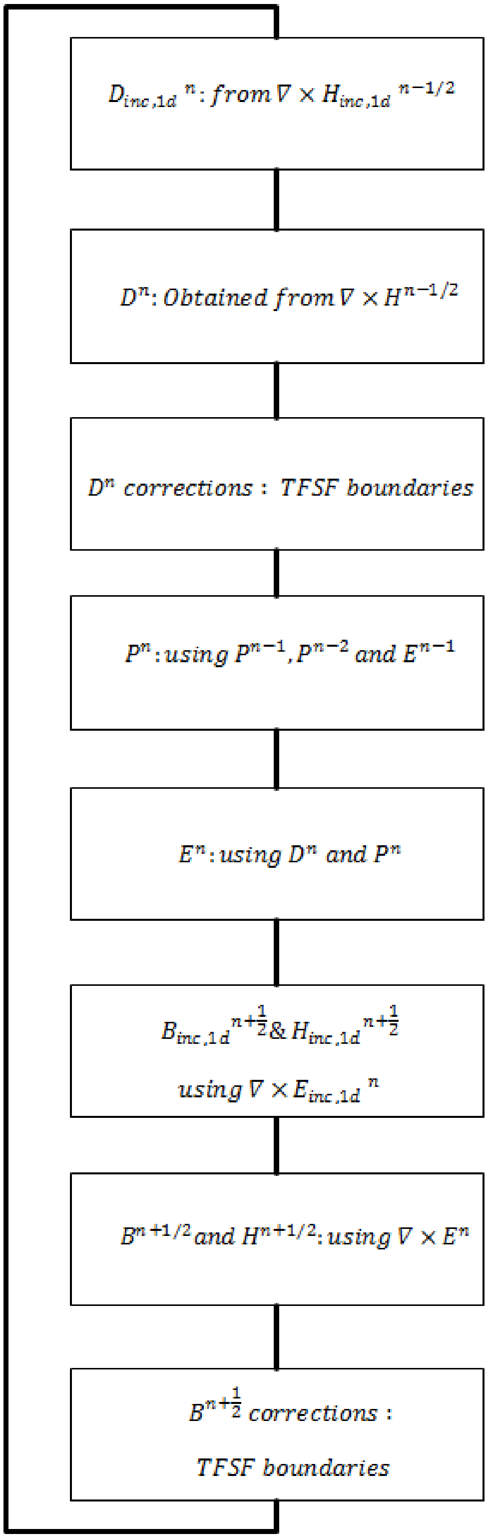

Figure 2-6 Flow Chart of TFSF boundary condition integrated in General ADE FDTD algorithm

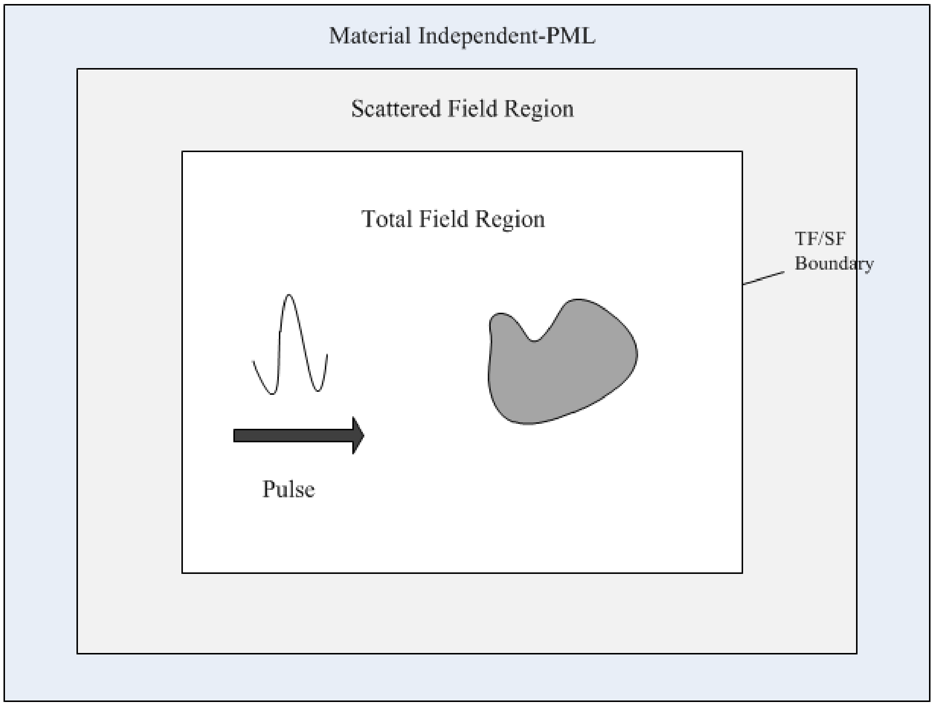

Figure 2-7 Computational Window

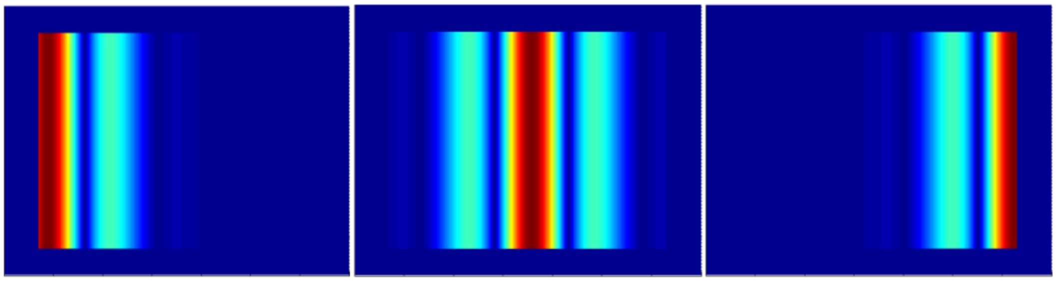

Figure 2-8 Propagation of plane wave without any scatterer with TFSF boundary condition notice no leakage in Region A

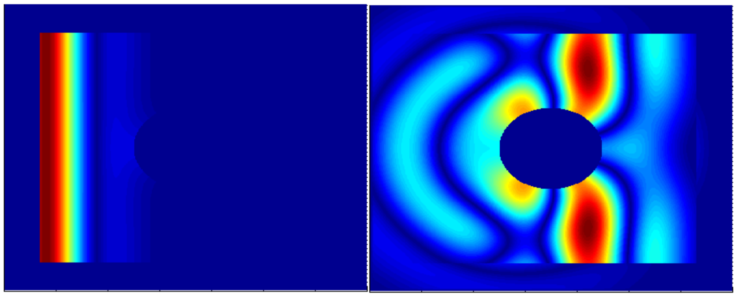

Figure 2-9 Propagation of the wave with a circular scatterer, notice scattered wave Region A

Chapter 3

M-I-M WAVEGUIDE COUPLED PLASMONIC RING RESONATORS

This chapter investigates the MIM waveguide coupled plasmonic ring resonator and ring resonator based devices for sensing. Properties of sources and the parameters measured will be discussed and followed by devices' detailed characterization and verification for their sensing properties. Ring resonator with a grating structure is one of the devices that is investigated for a sensitive configuration using parameters like sensitivity, Figure-of Merit and Limit of detection.

3.1 Introduction

The MIM waveguide coupled ring resonator is a plasmonic device with the etched out from a plane metallic film (*silver)* with a circular shape (representing a ring) and a rectangular shape(representing the MIM waveguide) and replaced with a dielectric. The size of the ring is defined by two radii inner (R_1) and outer radius (R_2) of silver and the average radius ($R_{ave} = (R_1 + R_2)/2$).The width if the M-I-M waveguide has a fixed width of $d = 50nm$ and it is placed at a fixed distance of $w = 5nm$. Silver (Ag) is modeled using the 6-pole Lorentz-Drude model. The core (dielectric) of the MIM ring resonator and the waveguide is of refractive index of unity (*air*).

The response of the MIM ring is verified using its dispersion relation. It is verified using the transmittance of the device.

Transmittance is defined as

$$Trasmittance = 10\log_{10}\frac{P_2}{P_1} \tag{3.1}$$

where P_1 and P_2 are the input and output power of the device (Figure 3-1)

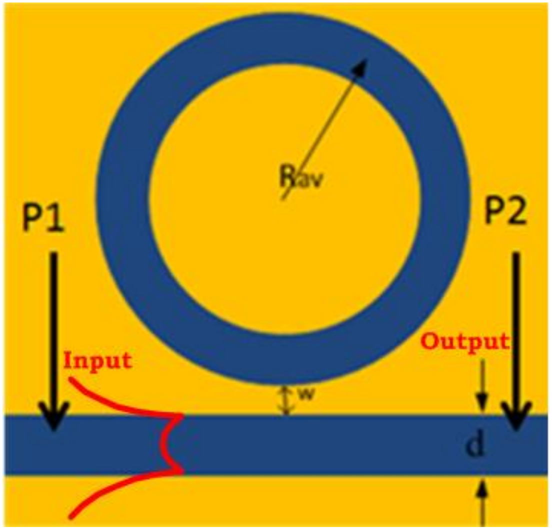

🟨 Metal (*Ag*) 🟦 Dielectric (*Air*)

Figure 3-1

The input to the MIM waveguide is a symmetric mode of the waveguide as shown in Figure 3-2

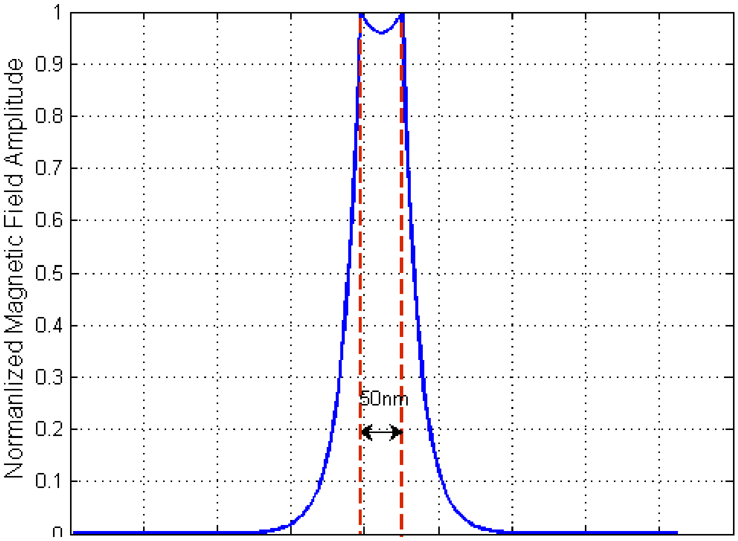

Figure 3-2 Mode of the MIM waveguide. The dashed line represents the waveguide boundaries

This mode is modulated with a gaussian in time (equation 3.2 and Figure 3-3) signal centered at $\lambda = 600nm$ wavelength with $t_p = 0.5fs$ and $t_o = 3t_p$

$$\text{source pulse(t)} = \exp\left(\frac{t - t_o}{t_p}\right)^2 \cos\left(\frac{2\pi}{\lambda}(t - t_o)\right) \tag{3.2}$$

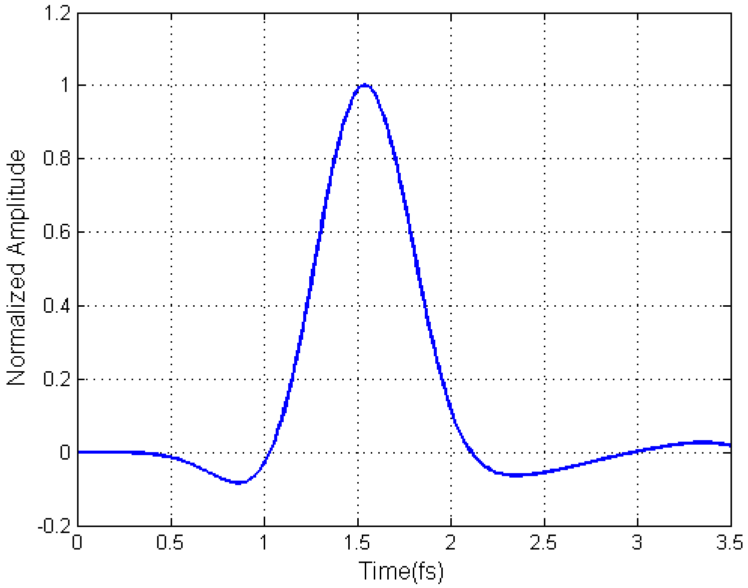

Figure 3-3 Gaussian in time pulse modulated with cosine.

Figure 3-4 is the spectrum of the signal which covers almost the entire optical domain. The input signal is wide-band so that all the possible modes in the optical domain can be excited in the ring resonator.

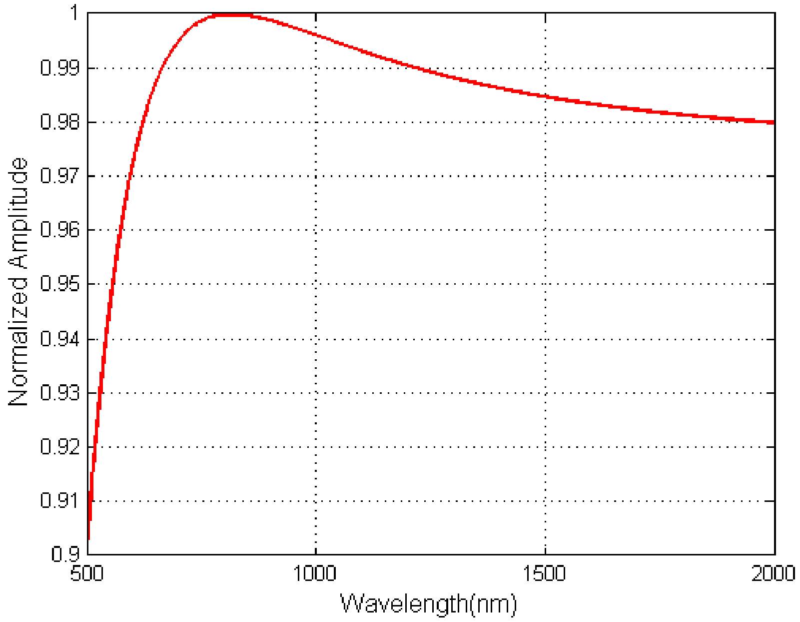

Figure 3-4 Spectrum of the Gaussian pulse.

The transmittance of the device would for a $R_{ave} = 170nm$ device with a width of $50nm$ is as shown in the Figure 3-5

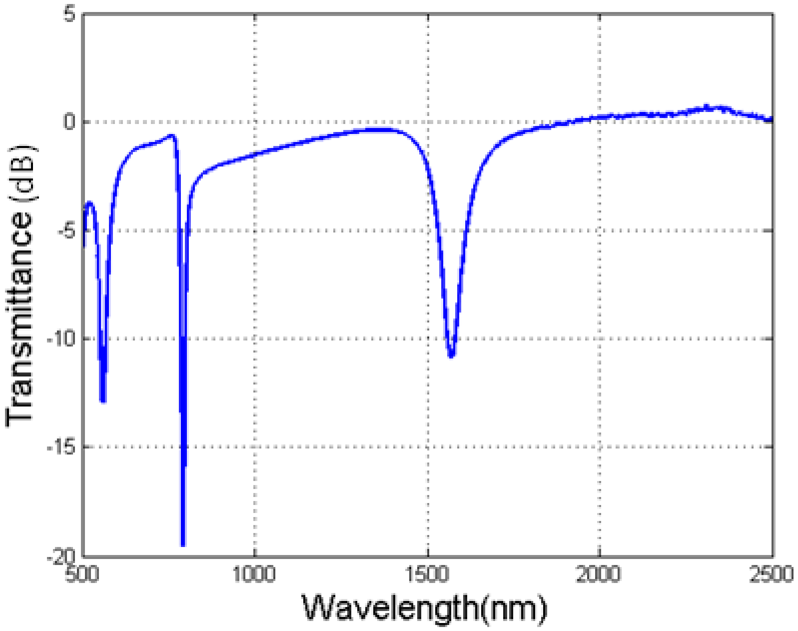

Figure 3-5 Transmittance of a ring with R_{ave} 170nm and width of $50nm$

It is noticed from the Figure 3-5 that the transmittance falls to a minimum at more than one wavelength. These are the various modes at which the ring resonates and filter these wavelengths out. Figure 3-6 shows the modes of the device with varying radius (R_{ave}) calculated using FDTD and its dispersion relation.

$$\frac{J_n'(kr_2)}{J_n'(kr_1)} - \frac{N_n'(kr_2)}{N_n'(kr_1)} = 0 \qquad 3.3$$

where r_2 is the outer radius and r_1 is the radius of the inner circle. J_n is a Bessel function of first-kind and order n and N_n is a Bessel function of second kind and order n. J_n' and N_n' are the derivatives of Bessel functions with respect to kr where k is dependent on the effective refractive index of the core of the ring.

As it was mentioned, bio-material binding changes the refractive index. Here the refractive index of core of the ring assumed to be bio-material is incremented in steps of $10^{-2} Refractive\ Index\ Units\ (RIU)$ starting from 1.01 and up to 1.09 RIU. Figure 3-7 shows how the response of a ring with $R_{ave} = 170nm$ is affected.

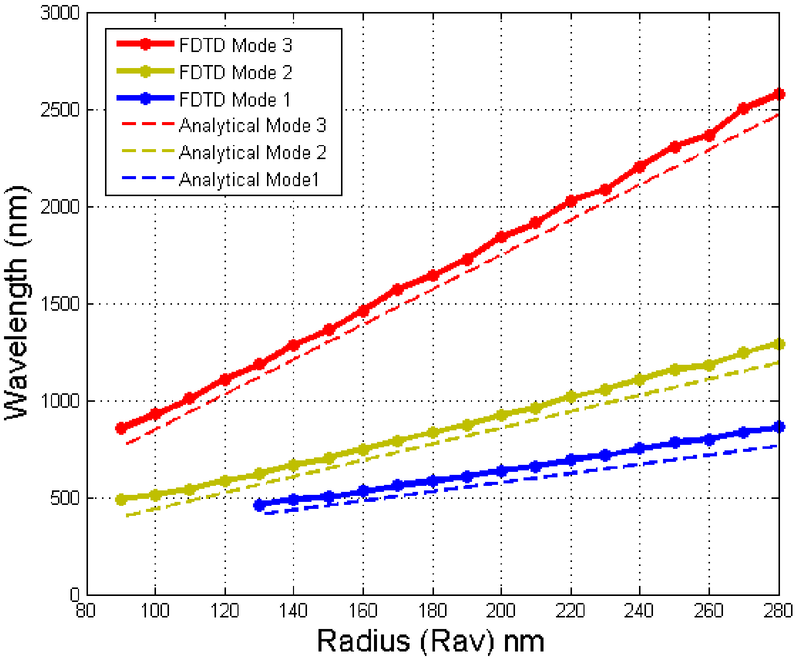

Figure 3-6 Resonance wavelengths for first three modes vs radius

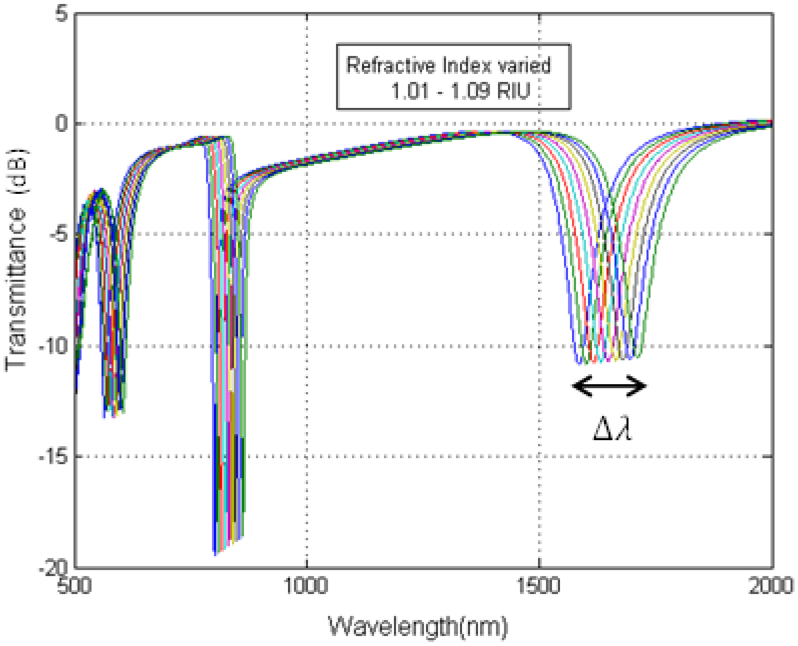

Figure 3-7 Transmittance with varying refractive index of the core with $R_{ave} = 170nm$

There is a red shift in the response of the device with increasing refractive index from 1.01 to1.09. This methodology is followed in the subsequent simulations to characterize and investigate the sensing properties of the device. The sensitivity of the device is defined as change the ratio of change in the resonant wavelength to change in refractive index. In this thesis the modes which lie in the near infra-red region are.

3.2 Basic M-I-M Plasmonic ring resonator

The M-I-M waveguide is placed very close to the ring resonator; it is placed at a distance of $w = 5nm$. The distance is close enough so that there is maximum coupling between the waveguide and the ring resonator as it is seen from Figure 3-2 the field strength of the mode decreases exponentially with distance. The mode which lies in the infrared region and close to optical communication wavelengths is investigated.

Effect of ring width on sensitivity

The effect of ring size (R_2) and width $(R_2 - R_1)$ on sensitivity is investigated. The inner radius (R_1) is varied from close to zero to radius close to that of the outer ring (R_2). As shown in the Figure 3-8 with increasing width of the ring the sensitivity of the ring decreases. The mode which is in the infrared region is investigated here.

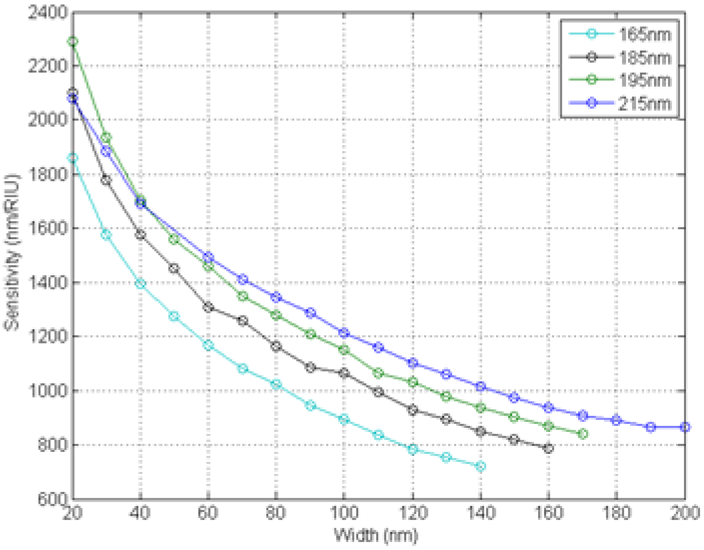

Figure 3-8 Sensitivity vs. width of the ring for increasing outer radii (R_2) of mode in infrared region

It is to be noted here that with increasing outer radius (R_2) the sensitivity of the device increases. From this it can be concluded that larger ring size (R_2) with smaller width gives better sensitivity.

Effect of Ring Width on Full Wave Half Maximum

Full wave half maximum of the device is investigated and how it varies with width ($R_2 - R_1$) and varying outer ring radius (R_2). It is seen from Figure 3-9 that with increasing thickness the FWHM decreases.

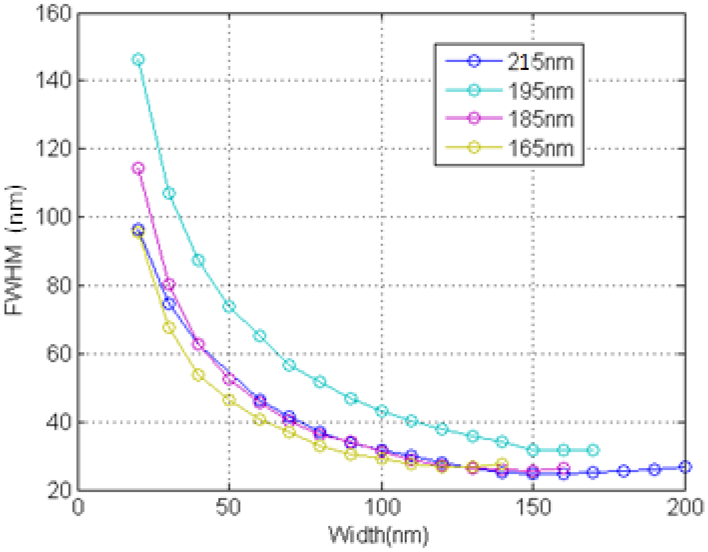

Figure 3-9 FWHM vs width with varying outer ring radius

Effect of Ring Width on Figure of Merit

The figure of merit of the device is found using FWHM and the sensitivity Figure 3-10. It is seen that the FoM values show an increasing trend up to a certain width but stabilizes after it reaches a certain width, again to decrease slightly with increasing width. FoM values are inversely dependent on the FWHM of the signal as it is seen from the previous figures the FWHM decreases with width leading to better FoM values at higher widths of the device.

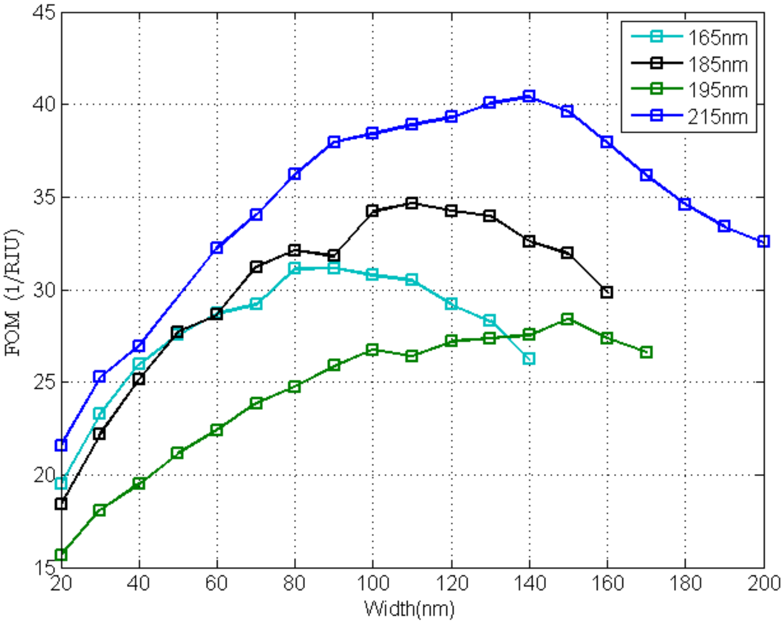

Figure 3-10 FoM vs width

Real Time Sensing

Limit of Detection (LOD) is defined before as the smallest amount of change in the refractive index that the device can detect. To calculate LOD of the device, first an optimized device is chosen according to the radius and the width of the device. The sensitivity is decided using the FoM calculations as shown in Figure 3-10. A device with considerable sensitivity is chosen and a continuous sinusoidal signal at the resonant wavelength of the ring is input to the device and the output (transmitted) power is measured.

The following are the device parameters that are chosen for this real-time test. The inner radius of the ring is $135nm$ and the outer radius is $215nm$ ($R_{ave} = 175nm$) and the width of the device is $80nm$ and a resonant wavelength is at $1343.8nm$ for a core refractive index of 1.01

The MIM mode of the waveguide is modulated with a continuous sinusoidal wave at $1343.8nm$ and the output power is calculated and its envelope is plotted as shown in Figure 3-11.

To simulate binding the refractive index of the core is increased from 1.01 linearly with time after the output power stabilizes and reaches a steady value the initial. The device takes time before it transmits a steady output power as the plasmonic resonator takes time to resonate due to a relaxation associated with the plasmonic properties of the metal and the resonator itself. It is seen that the ring resonator is taken off resonance and there is an increase in the output power. It increases nearly linearly with increase in the refractive index. This increase in output power is seen only up to a refractive index of 1.063. Further increasing the refractive index, the nearly linear increase of output power is disturbed and this puts a limit up to which the device can detect refractive index change which is 1.063.

The refractive index is increased with a rate of $8.9286 \times 10^{-4} RIU/fs$ to this rate the output power changes by a rate of $3.384W/fs$. Finding the ratio of rate of change of refractive index to rate of change of power would give the refractive index change that is required for change in $1W$ output power. This value is $2.637 \times 10^{-4} RIU/W$

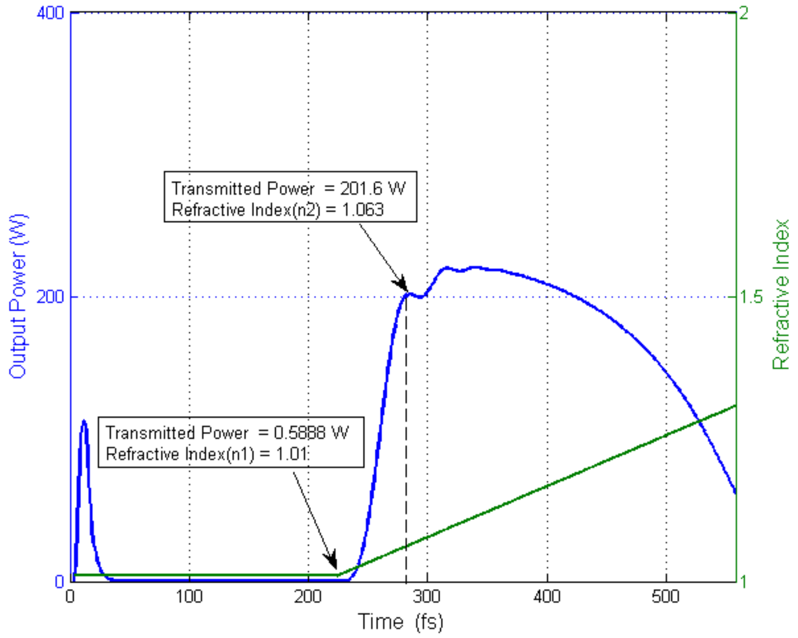

Figure 3-11 Real-time test with linearly varying refractive index with time

3.3 Basic M-I-M Plasmonic ring resonator with gratings

The previous device which was tested is a simple ring structure. The next device that is investigated is a ring with grating. As grating are periodic structures period of the grating is defined in terms of angle which it sub-tends at the center of the ring and also the duty cycle of the device (Figure 3-12)

θ is defined as the period of the grating and the duty is defined as equation 3.4

$$duty\ cylce = \frac{\alpha}{\theta} \qquad 3.4$$

where α is the angle which a single cycle of the dielectric material subtends on the center of the ring as shown in the Figure 3-12

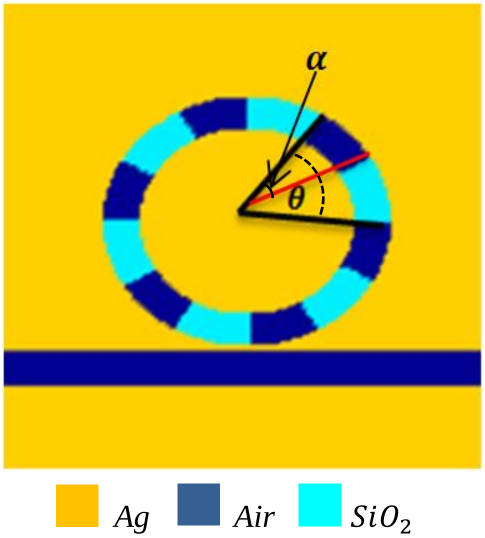

Figure 3-12 MIM ring resonator with grating

Introduction of grating in the core of the MIM ring drastically alters the response of the ring. The gratings that are introduced are of SiO_2 with refractive index of 1.45 with a period of 40^o and duty cycle 0.5 ($\alpha = 20^o$ and $\theta = 80^o$) is introduced. The following Figure 3-13 shows the response of the ring changes with and without gratings. Without changing the size or the width of the ring the response of the device can be changed.

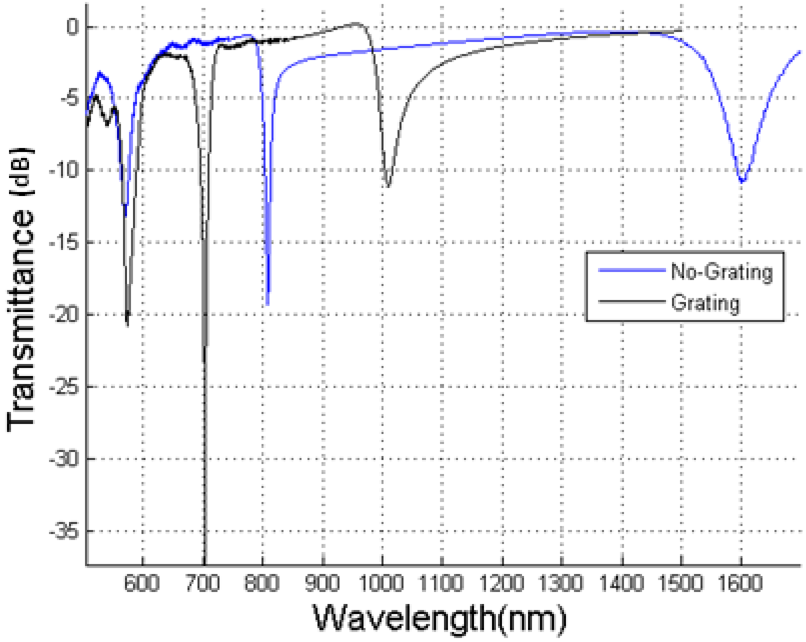

Figure 3-13 Plot of transmittance spectrum of resonator without grating and with a grating of period 40^o and duty cycle 1.0

By keeping the period constant the duty cycle of the grating is varied and with increase in the duty cycle from 0.5 (grating) to 1.0 (no grating) there is a blue shift in the response of the device as seen in the Figure 3-14.

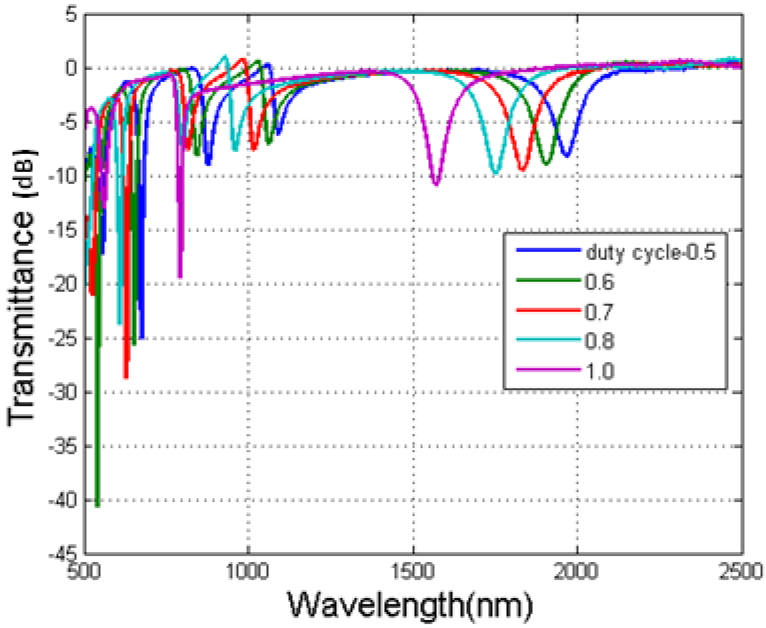

Figure 3-14 Transmittance of the ring with varying duty cycle and fixed period of 40^o

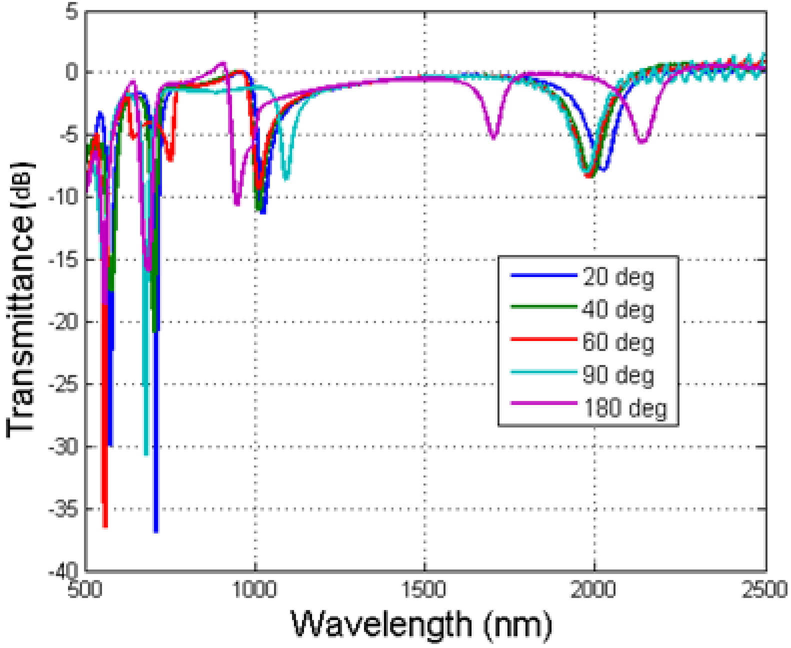

Figure 3-15 Transmittance of the device with varying period and duty cycle of 0.5

The device is also tested for varying period with fixed duty cycle of 0.5. The period is varied as $\theta = 20^o$, 40^o, 60^o, 90^o and 180^o. It is seen that response (Figure 3-15) of the device for angles 20^o to 90^o has a same general shape and there is a relatively small blue-shift in the resonance frequencies of the device than when compared to the variation in the duty cycle.

It is seen that by introducing grating the response of the device can be controlled without changing the size of the device. The gratings make the device highly tunable. The introduction of grating gives control over of the response of the device.

3.3.1 Bio-sensing using grating with period of 45^o

Another device that is tested is a grating based structure. The basic outlay of this device is that gratings are introduced in the ring and also a sensing region is introduced above the ring of width $50nm$ placed at a distance of $5nm$ (Figure 3-16).

The first device which is investigated is a ring with a grating with period of 45^o.

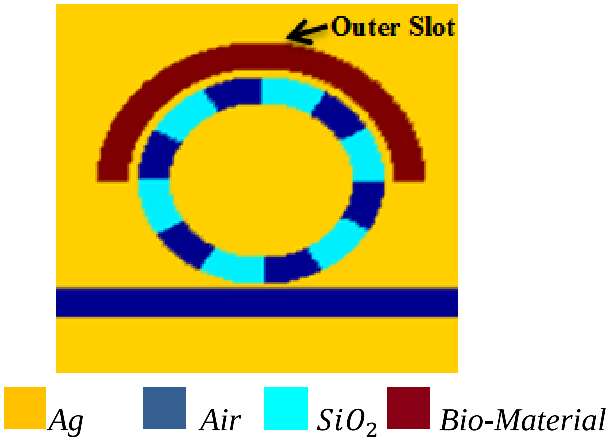

Figure 3-16 Outer slot is the sensing region area of the device

Effect of Ring Width on Sensitivity

The device is investigated for it sensitivity with varying width for fixed outer radius of the ring. It is seen from the Figure 3-17 that with increasing thickness the sensitivity of the device peaks at a certain thickness and slowly decreases with increase in thickness

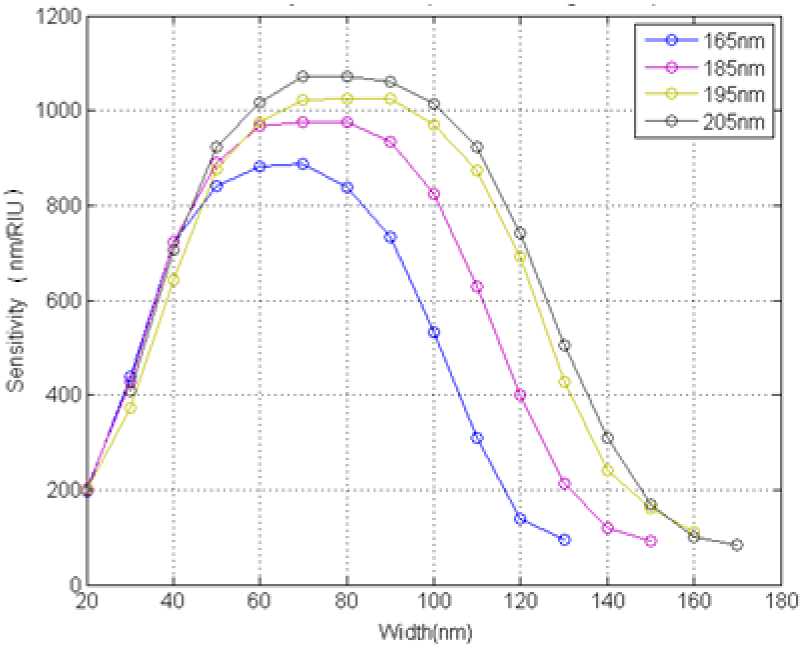

Figure 3-17 Sensitivity Vs. Width for varying outer radius of ring (R_2)

The general trend of sensitivity with respect to the thickness for a particular outer ring radius is that sensitivity increases and then decreases with increasing outer ring radius of the device. The increase in the sensitivity of the device is more pronounced with increasing thickness.

Effect of Ring Width on Full Wave Half Maximum

The next parameter that is measured is the Full-wave half maximum of the device with increasing thickness for varying outer radius of the ring. It is seen from the Figure 3-18 that the FWHM of the device decreases with increasing thickness of the device and also with increasing outer ring radius the FWHM also increases.

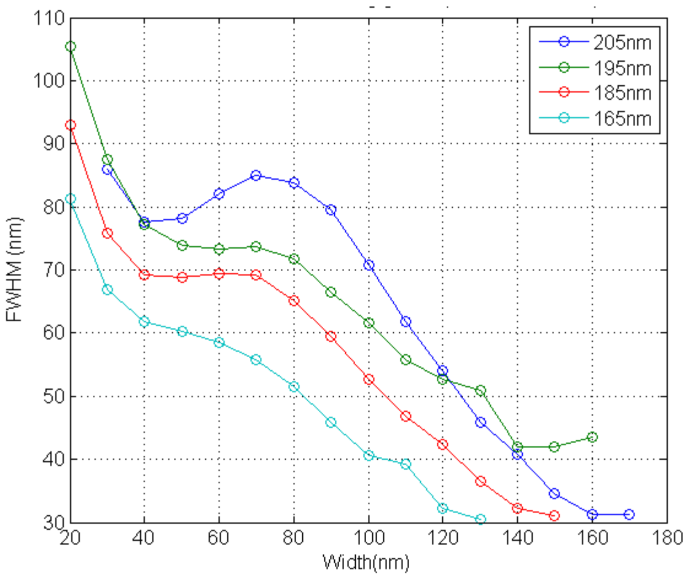

Figure 3-18 FWHM Vs. width with varying outer ring radius (R_2)

Effect of Ring Width on Figure of Merit

Figure of merit (FOM) of this device is calculated from the above sensitivities and FWHM. From Figure 3-19 it is seen that FOM increases with increasing thickness but decreases after it reaches a maximum value. From this it can be concluded that the smaller size rings and with thickness around $80nm$ are better sensors.

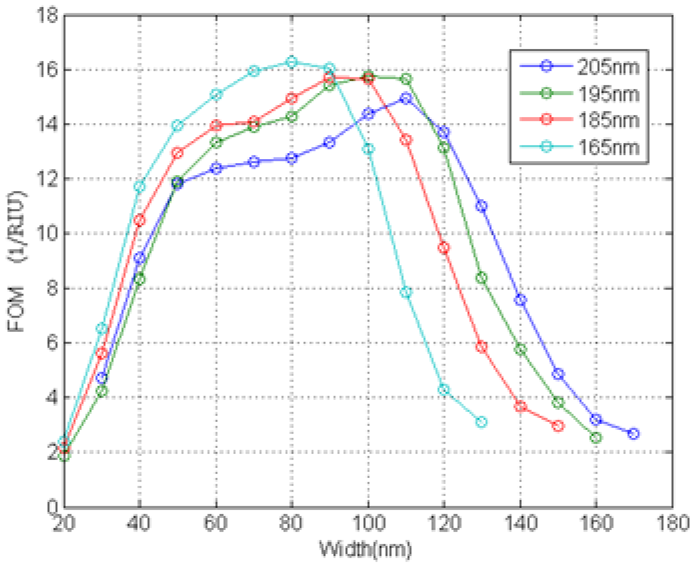

Figure 3-19 FoM Vs Width for varying radius (R_2)

Real-Time Sensing

The following device parameters that are chosen for this real-time test; inner radius (R_1) of the ring is $85nm$ and the outer radius (R_2) is $165nm$ ($R_{ave} = 145nm$), the width of the device is $80nm$ and a resonant wavelength is at $1210nm$ for a core refractive index of 1.01. The MIM mode of the waveguide is modulated with a continuous sinusoidal signal at a wavelength of $1210nm$ and the output power is calculated and its envelope is plotted as shown in Figure 3-20. To simulate binding the refractive index of the core is increased from 1.01 linearly with time after the transmitted power reaches a steady value. The device takes time before it transmits a steady output power as the plasmonic resonator takes time to resonate due to a relaxation associated with the plasmonic properties of the metal and the resonator itself. It is seen that the ring resonator is taken off resonance and there is an increase in the output power. It increases near linearly with increase in the refractive index. This increase in output power is seen only upto a refractive index of 1.168 and on further increasing the index the near linearity in increase of output power is disturbed. This device has a wider range the simple MIM ring resonator.

The refractive index is increased with a rate of $8.9286 \times 10^{-4} RIU/fs$ to this rate the output power changes by a rate of $0.358W/fs$. Finding the ratio of rate of change of refractive index to rate of change of power would give the refractive index change that is required for change in $1W$ output power. This value is $2.493 \times 10^{-3} RIU/W$.

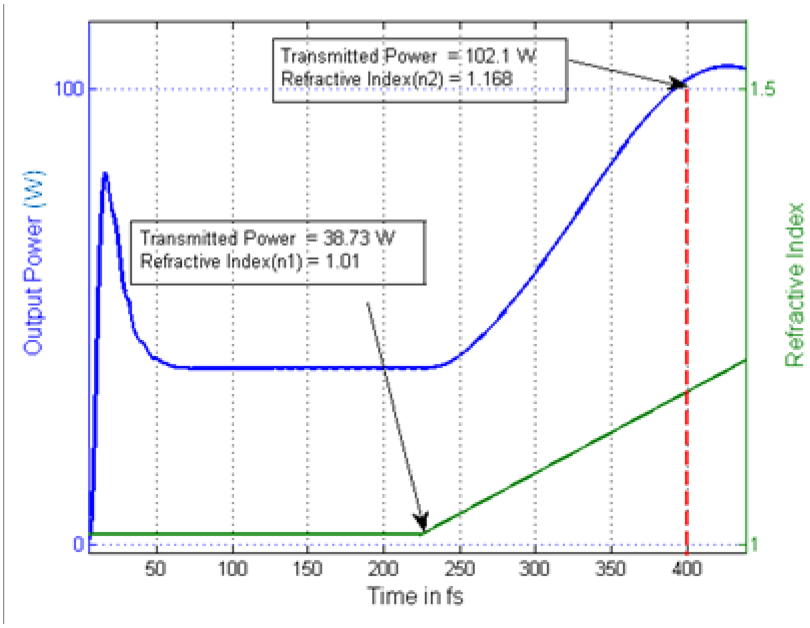

Figure 3-20 Real Time analysis with linearly varying refractive index with time

3.3.2 Bio-sensing using grating with period of 90^o

The second device that is tested based on the grating inside the ring resonator is that of period of 90^o.

Effect of Ring Width on Sensitivity

The device is investigated for the effect on sensitivity with varying width of the device for varying outer ring radius(R_2) of the device. As seen Figure 3-21 the general trend in sensitivity of the device is that it increases with width but reaches a maximum value and then decreases with increase in the width of the ring.

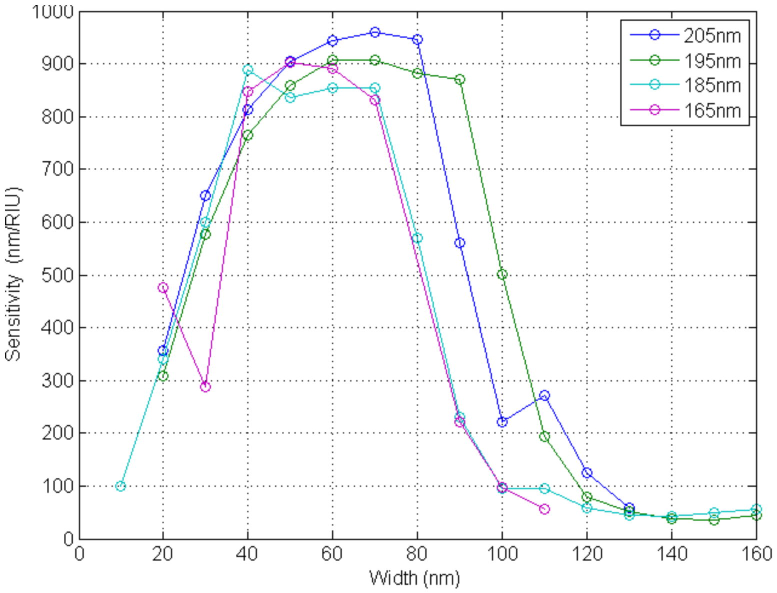

Figure 3-21 Sensitivity Vs. Width for varying refractive index

Effect of Ring Width on Full Wave Half Maximum

The full wave half maximum (FWHM) of the device with grating period 90^o is measured. Figure 3-22 shows that FWHM sees no drastic change with increasing width initially but there is a sharp fall in $60nm$ and then it is relatively unchanged when the width is further increased.

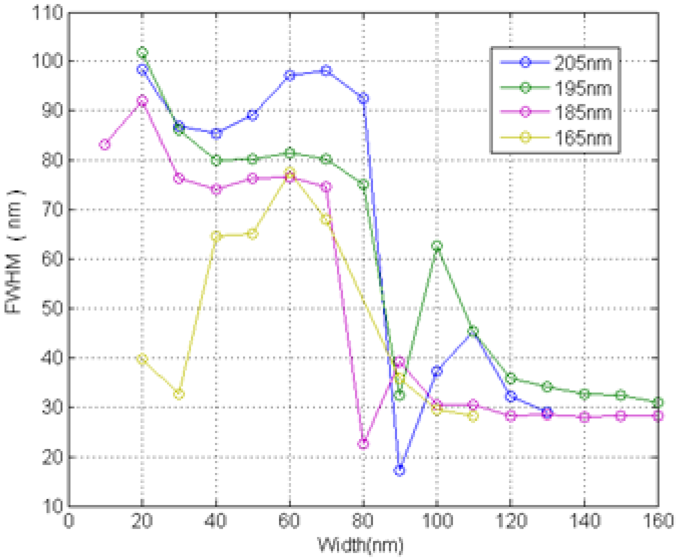

Figure 3-22 FWHM vs width with varying outer ring radius (R_2)

Effect of Ring Width on Figure of Merit

The FoM is calculated for varying width for different outer ring radius. As seen in Figure 3-23 there is a sharp increase in the FOM after the width reaches a particular value and then decreases to be constant with increasing thickness and there is increase in FoM values with increasing size of the ring

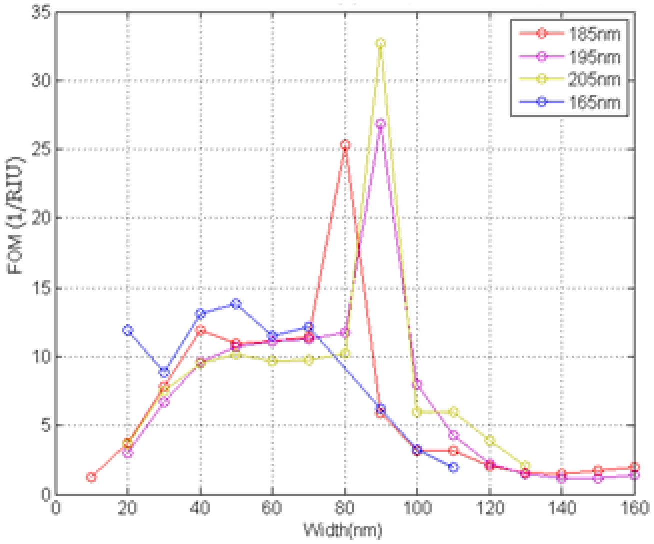

Figure 3-23 FoM vs width with varying outer radius (R_2)

Real-time Sensing

The following device parameters are chosen for this real-time test; The inner radius of the ring is $115nm$ and the outer radius is $205nm$ ($R_{ave} = 160nm$) and the width of the device is $80nm$ and a resonant wavelength is at $1275nm$ for a core refractive index of 1.01.The MIM mode of the waveguide is modulated with a continuous sinusoidal wave at $1275nm$ and the output power is calculated and its envelope is plotted as shown in Figure 3-24.To simulate the binding the refractive index of the core is increase from 1.064 linearly with time. As it is seen, the ring resonator is taken off resonance and there is an increase in the output power, and it increases in a near linearly with increase in the refractive index. This increase is output power is seen only up to a refractive index of 1.213 and on further increasing the index the near linearity in increase of output power is disturbed. This device has a wider range than the one with period of 45^{o} and the simple MIM ring.

The refractive index is increased with a rate of $8.9286 \times 10^{-4} RIU/fs$ to this rate the output power changes by a rate of $0.2626W/fs$. Finding the ratio of rate of change of refractive index to rate of change of power would give the refractive index change that is required for change in $1W$ output power. This value is $3.4 \times 10^{-3} RIU/W$.

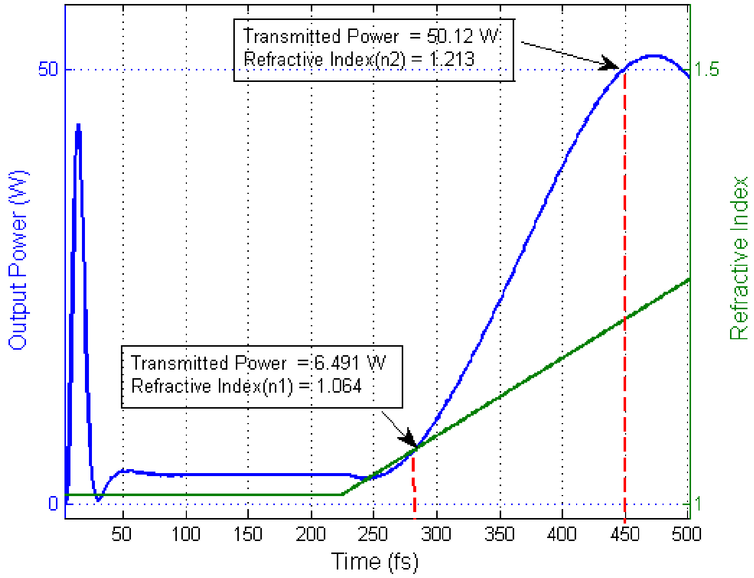

Figure 3-24 Real Time analysis with linearly varying refractive index with time.

Summary and Discussion

Three devices based on the plasmonic ring resonator have been tested and investigated for their sensitivity and Figure of Merit.

- For the simple MIM ring resonator it is seen that with increasing width of the ring the sensitivity of the device decreases. Also, with increasing size (outer radius R_2) the sensitivity increases and also the sensitivity of the device varies from around $2000nm/RIU$ to around $800nm/RIU$. The FWHM also decreases with width of the device but there is no substantial change with increasing size. This leads to FoM, which increases up to a certain width and then decreases with increasing width and among the four radii tested it is seen that the device has a better FoM with increasing size.
- When a real time test is done to this device the Limit of Detection was found to be $2.637 \times 10^{-4} RIU/W$ and the range in which it can operate linearly was found to

be $0.053RIU$. This run was done using a sinusoidal carrier of wavelength $1343.8nm$

- For the MIM ring with a grating of period of 45^o the sensitivity increased with increasing width up to a certain width but then decreases with increasing width and with increasing size the sensitivity increases The sensitivity of the device varies from less than $200\,nm/RIU$ to reaching a maximum around $1100\,nm/RIU$. The FWHM decreases with increasing width and also decreasing size and FOM increases with decreasing size of the device and increases with width up to a certain maximum value and then starts to decrease with more increase in width. This is in complete contrast to the simple ring where bigger size of the device gave better FOM though the FOM values when compared to the simple ring were less.
- Real-time test was done and it was found that the Limit of Detection was $2.493 \times 10^{-3}RIU/W$ and the range at which it can operate was $0.1580\ RIU$. This run was done using a sinusoidal carrier of wavelength $1210nm$ and the outer radius of the device was $165nm$.
- From the above two results it can be concluded that with the introduction of grating inside an MIM ring resonator helps in tuning the resonant wavelength of the device and also larger wavelengths (infrared close to telecommunication wavelength) are obtained for smaller devices than when compared to the simple ring. Thus giving an advantage in reducing the size of the device. Though the MIM ring with grating is less sensitive and has a relatively less FOM but these are good enough for changes in refractive index of the order of $10^{-3}RIU/W$

Chapter 4

EMITTER COUPLED PLASMONIC NANO-PARTICLE RESONATOR

This chapter investigates the sensing properties of plasmonic nano-particles which are coupled to emitters. This chapter investigates the twin sensing capabilities of the sharp emission spectrum of the emitter and also the sensitive nature of the plasmonic nano-particle. In this chapter the nano-particles configuration is designed such it resonates at the emitter wavelength. This structure then is optimized for distance of the source from the nano-particles and investigated for sensing.

4.1 Scattering properties of nano-particles

In gold or silver nano-particles, if excited properly surface plasmons are generated. These surface plasmons are confined to the surfaces of the metal nano-particles. These are called localized surface plasmons (LSP) as opposed to the surface plasmon that are excited on metal dielectric interface which are propagating surface plasmons.

These localized surface plasmons are extremely sensitive to the shape and size of the nano-particles and also the environment that they are placed in. When the natural oscillation frequency of the plasma inside the particles match with that of the external excitation leads to resonance called as the Localized surface plasmon resonance (LSPR).

When a LSPR is excited there is huge enhancement in the near field intensity of the nanoparticles and this also shows in the far-field characteristics of the particles. The power scattered by these particles in the far-field is more at the resonant wavelengths than off resonance wavelengths.

This property of the nanoparticles is used to find the resonant wavelengths of the nano-particles. TFSF is used to find the scattered field response of the nano-particles. There are three parameters that define the scattering properties of the nano-particles. They are

1. Scattering
2. Extinction
3. Absorption

Suppose that the rate at which the detector receives the power is given by U in the presence of the particles and U_o if the particles are removed then if $U_o > U$ it is said that the presence of particles has resulted in extinction of the incident beam and if the particles are embedded in non-absorbing medium then the difference $U_o - U$ is accounted by *absorption* in the particles and *scattering* by the particles, or

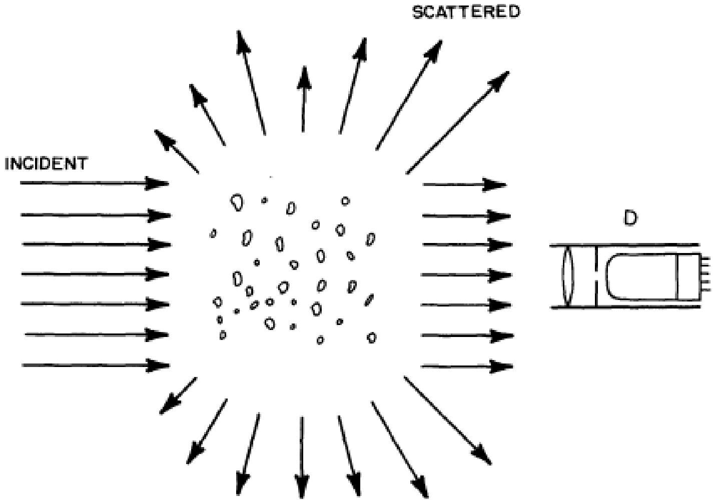

Figure 4-1 Extinction by collection of particles(adapted from[8]**)**

$$W_{ext} = W_{abs} + W_{sca} \tag{4.1}$$

Equation 4.1 gives the relation between scattered power, absorbed power and the power which undergoes extinction.

The common feature among power scattered, absorbed and extinction for a particular collection of particles is the frequency dependence. The maximum of any of these parameters occur at the same wavelength or frequency so calculation of one parameter gives the resonating wavelengths of plasmonic particles that are to be considered later.

The terms W_{sca} and W_{abs} are calculated by integrating the pointing vector over a closed surface as

$$W_{sca} = \oint_{S1} S_{sca}.\hat{n} \;\; dA \tag{4.2}$$

$$W_{abs} = \oint_{S2} S_{abs}.\hat{n} \;\; dA$$

S_{sca} is calculated using purely scattered electric(E_{sca}) and magnetic fields (H_{sca}) as ($E_{sca} \times H_{sca}$) normal to $S1$(using $\hat{n}$ unit vector normal to S1) which is a closed rectangular surface through the scattered field region. S_{abs} is calculated using total electric(E_{abs}) and magnetic fields (H_{abs}) as ($E_{abs} \times H_{abs}$) normal to $S2$ (using $\hat{n}$ unit vector normal to S2) which is a closed rectangular surface through the total field region and W_{ext} is calculated using equation 4.1.

When W_{ext} is divided with W_{inc} calculated with no particles present the term becomes scattering cross-section, absorption cross-section and extinction cross-section.

$$\sigma_{ext} = \frac{W_{ext}}{|\mathbf{S}_{inc}|} = \sigma_{abs} + \sigma_{sca} \qquad 4.3$$

4.2 Scattering Properties Verification –Single Nanoparticle case

For verification, scattering cross-section using FDTD and using analytical formulation (equation -1.66) of the scattering cross-section is calculated. The scattering cross-section of a silver nano-particle with a radius $25nm$ and $30nm$ placed in free-space is found. The input is a gaussian in time plane wave (Figure 4-2) centered at $600nm$. This covers the entire optical domain in the spectrum of the signal. As seen in Figure 4-3 the scattering cross-section calculated using FDTD and analytically have a very good matching for a mesh size $1nm$ and this improves further with decrease in mesh size ($0.5nm$) of the computational window as tested for the nanoparticle with $25nm$ the resonant wavelengths are $249nm$ and $358.6nm$ which are the two dominant modes (quadropole and a dipole respectively).It is also verified for radius $30nm$ (Figure 4-4)

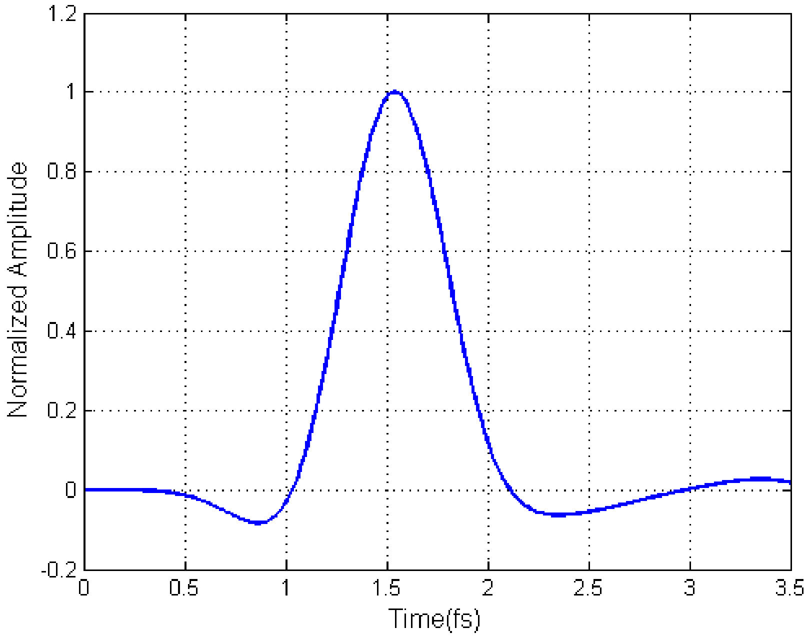

Figure 4-2 Gaussian in time modulated with a cosine pulse used as incident wave

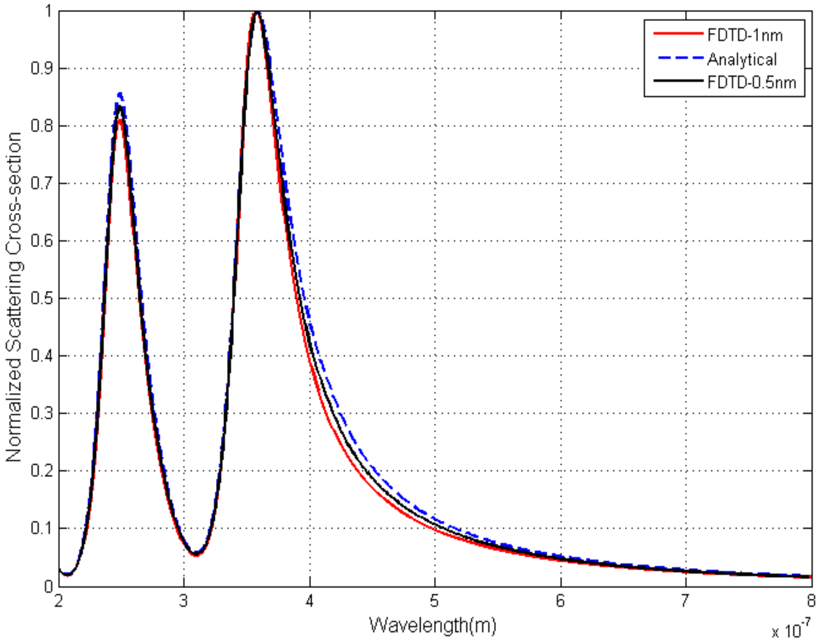

Figure 4-3 Normalized Scattering Cross-section vs Wavelength for 25nm radius Ag nanoparticle

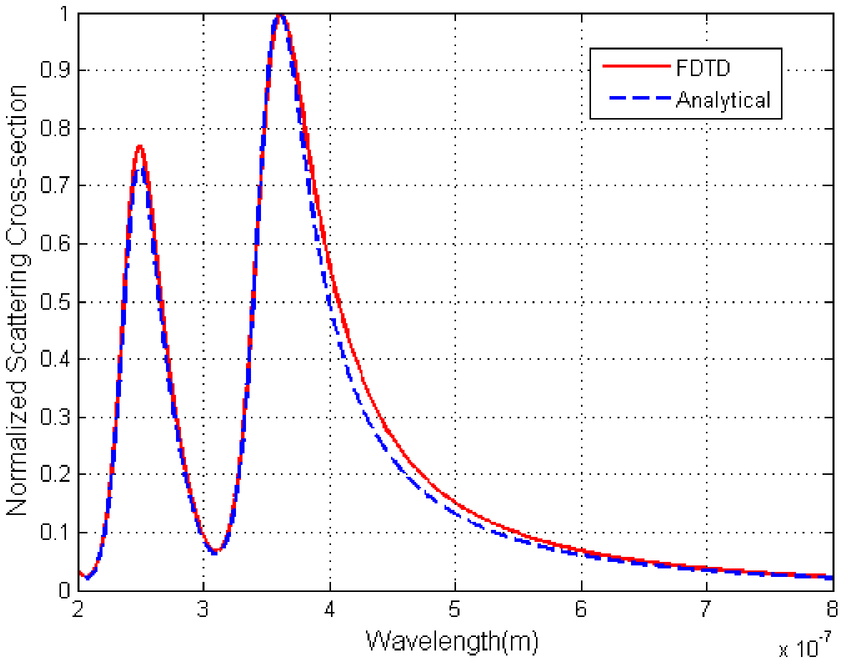

Figure 4-4 Normalized Scattering Cross-section vs Wavelength for 30nm radius Ag nanoparticle

This verifies the calculation of the resonant wavelength of the nanoparticles using FDTD and this can be employed for the calculation of scattering cross-section for various other configurations.

The active medium is doped with europium that emits at $595nm$ and $620nm$. The nano particles size, number of particles and its configuration is optimized so as to match its resonance with that of emission wavelength.

4.3 Device Optimization

The first step that is done in trying to find a suitable arrangement of nano-particles so that they resonate at the emission wavelength of europium (around $620nm$) is by increasing the number of particles and investigate how this effects the resonance.

The active device is based on the concept that the spectrum of the plasmonic nano-particles at resonant wavelength must be sharp, such that the device becomes extremely sensitive to changes in the refractive index and small change in the refractive index in the environment takes the particles off resonance.

Configurations with $2, 3, 4\ and\ 6$ silver nano-particles of radius $25nm$ strongly coupled (close enough so that the LSP strongly interact) equidistantly placed at a distance of $5nm$ from each other is tested. It is seen from the Figure 4-5 that the scattering cross-section of the particles have a red-shift with increase in number of particles and there is also broadening of the response.

The next parameter that is varied is the inter-particle distance. The inter-particle distance is decreased from $5nm$ to $3nm$. As seen in Figure 4-6 though the spectrum becomes sharper but with increasing the number of particles the spectrum of the scattering cross-section broadens.

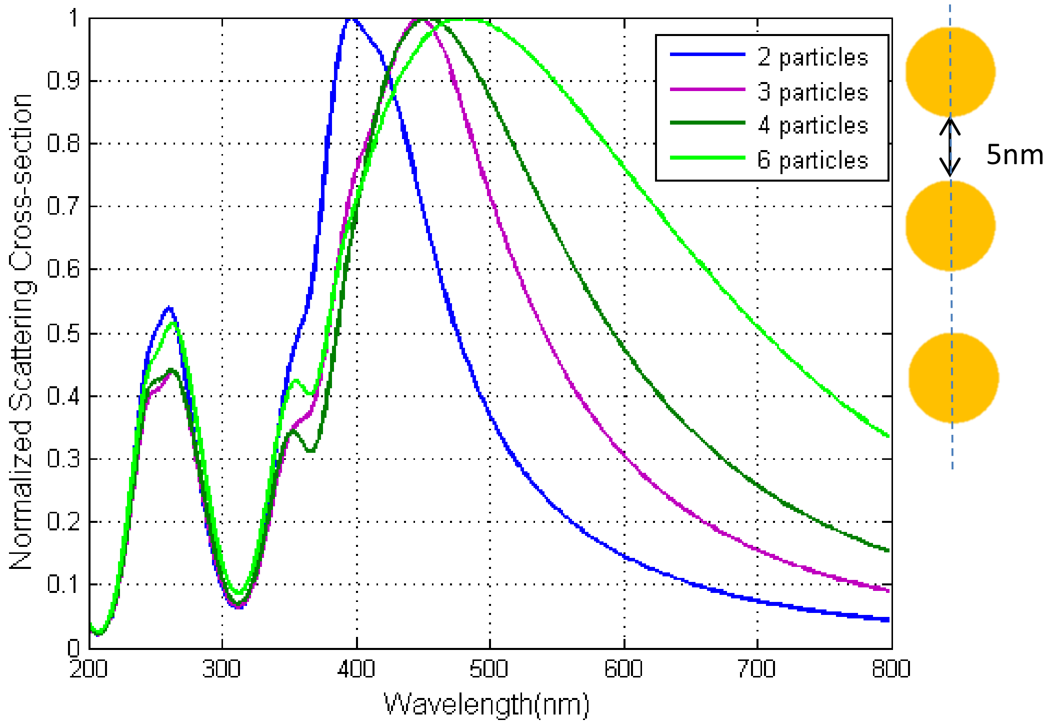

Figure 4-5 Two, three, four and six Ag nano-particles placed at distance of 5nm from each other

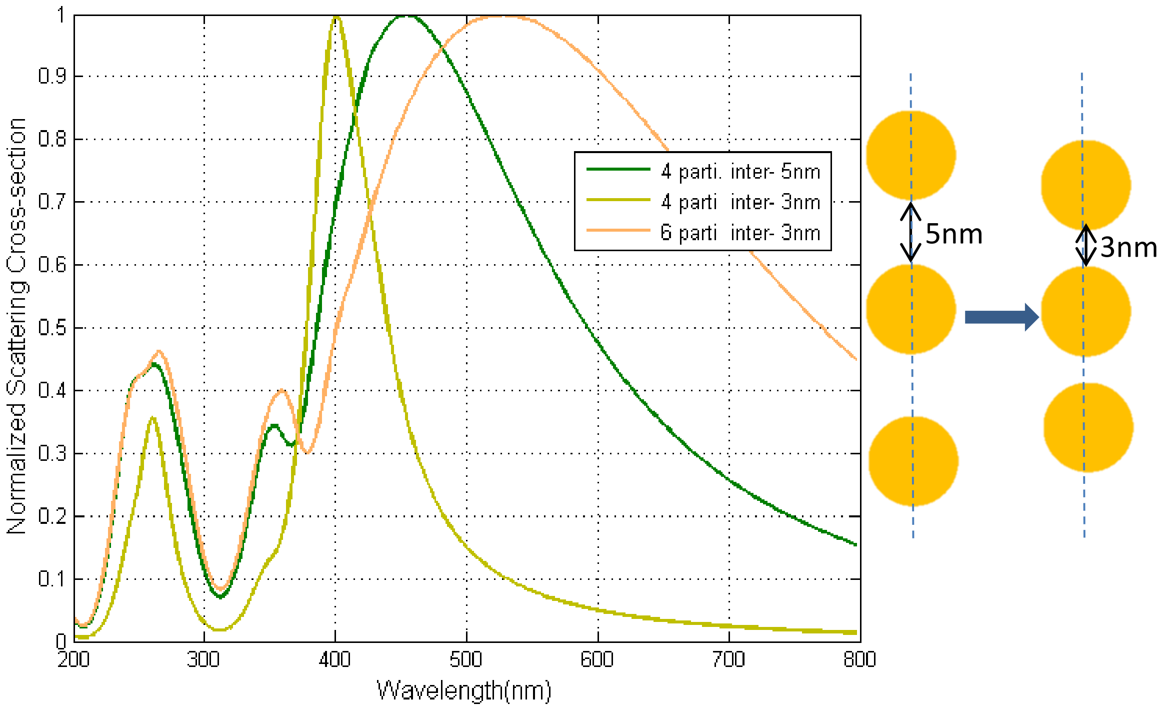

Figure 4-6 Four and six nano-particles with inter-particle distances 5nm and 3nm

The particles are also tested for a slightly uncoupled case where they are place at a distance of $10nm$ from each other for a 2 particle case. As seen from Figure 4-7 increasing inter-particle distance the spectrum does a little blue shift for the dipole mode and it is sharper than the strongly coupled case. This is due to the particles being weakly coupled and the individual response of the particles dominating the spectrum.

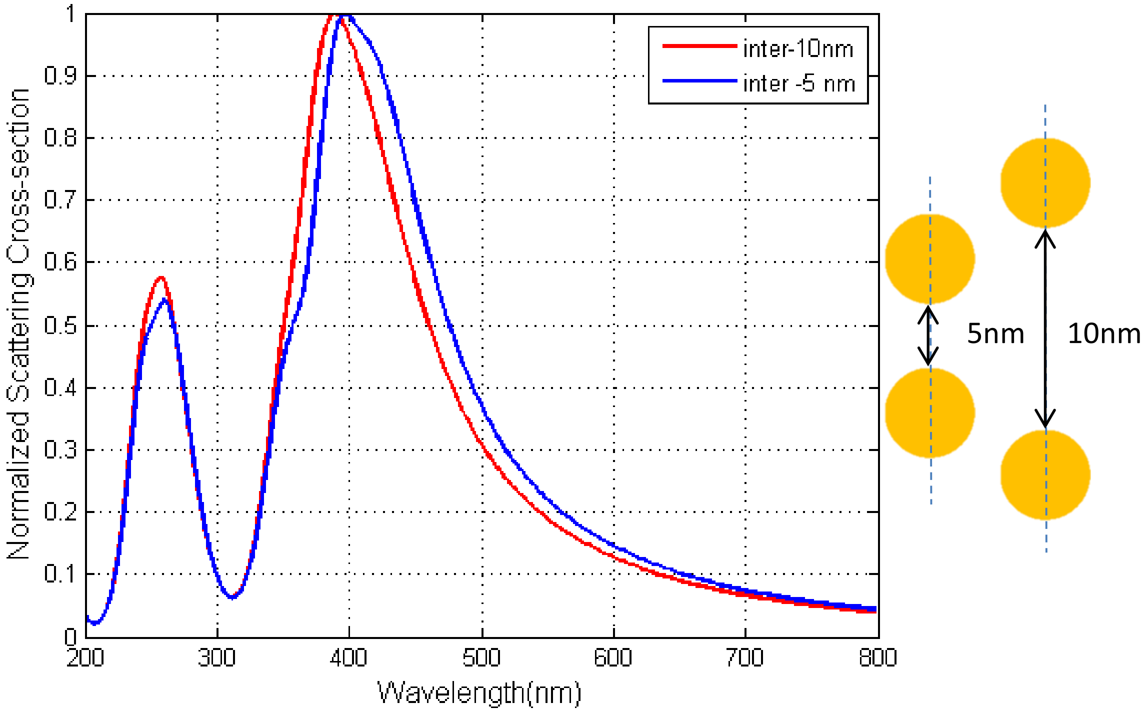

Figure 4-7 2 Particles for a strongly coupled and weakly coupled 2 nanoparticles with radius 25nm

Another parameter that can be varied is the dielectric constant of the medium in which the particles are embedded. The particles are finally needed to be embedded inside a medium. The medium is YVO_4 which is doped with Eu^{+3}. With the introduction of dielectric there is a red-shift in the response of the particles.

The following Figure 4-8 shows the response of a $20nm$ radius nano-particle in medium with refractive index 1.0 and the other response is with (YVO_4) with refractive index of 1.92.

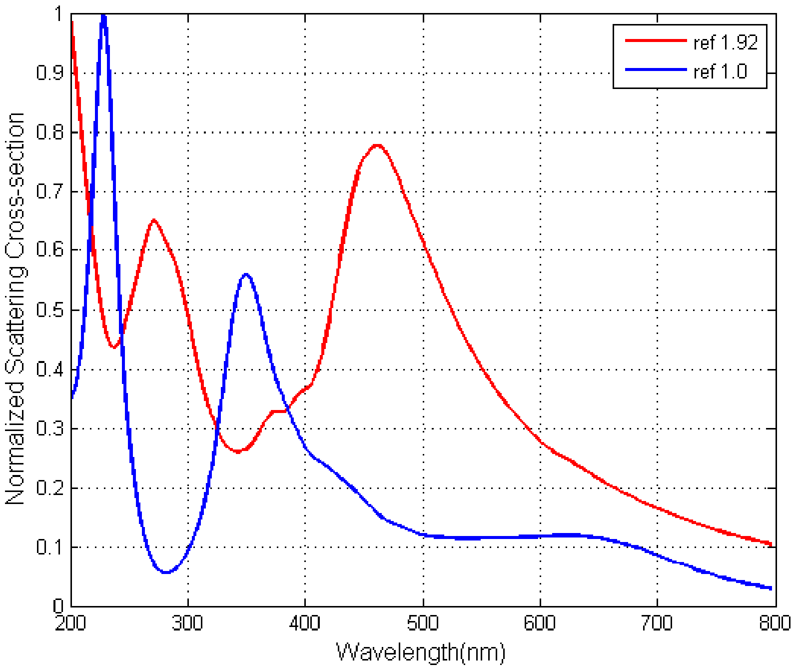

Figure 4-8 20 nm radius particle in medium with refractive index of 1.0 and 1.92

With this experience in hand regarding the behavior of the particles a configuration has been reached which has a resonance at $611.8\,nm$ which is close to the europium's emission wavelength. Six particles with radius $25\ nm$ and equidistantly place at $20nm$ is used. Figure 4-9 gives one of the resonances at $611.8nm$ as shown in Figure 4-10. The response at $611.8\,nm$ is sharp. When the scattering cross-section is found it is assumed that there is no biomaterial so the refractive index in that region is 1.0.

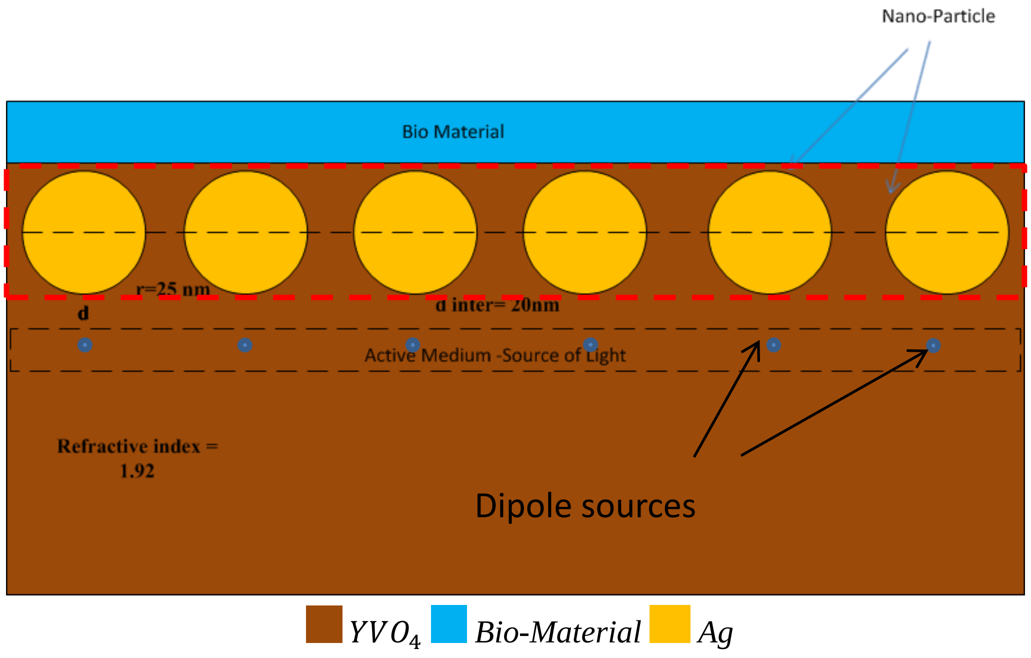

Figure 4-9 Active Device with biomaterial and weakly coupled nano-particles.

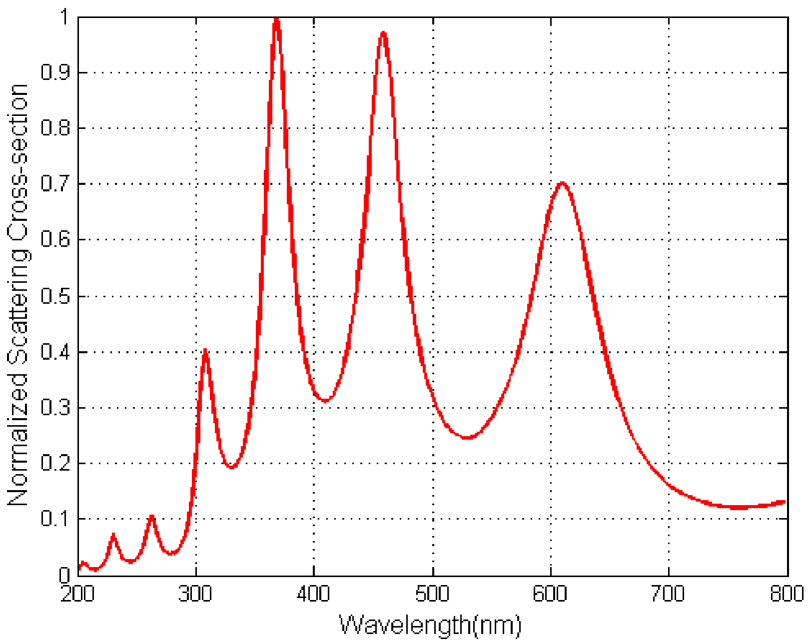

Figure 4-10 The scattering cross-section of the above described configuration.

4.4 Bio-sensing Characteristics of the proposed device

The nano-particles have been optimized to be coupled to source wavelength. The emitter is assumed to be a dipole centered at $611.8nm$. The emitter is a very narrow-band signal as shown in Figure 4-11.

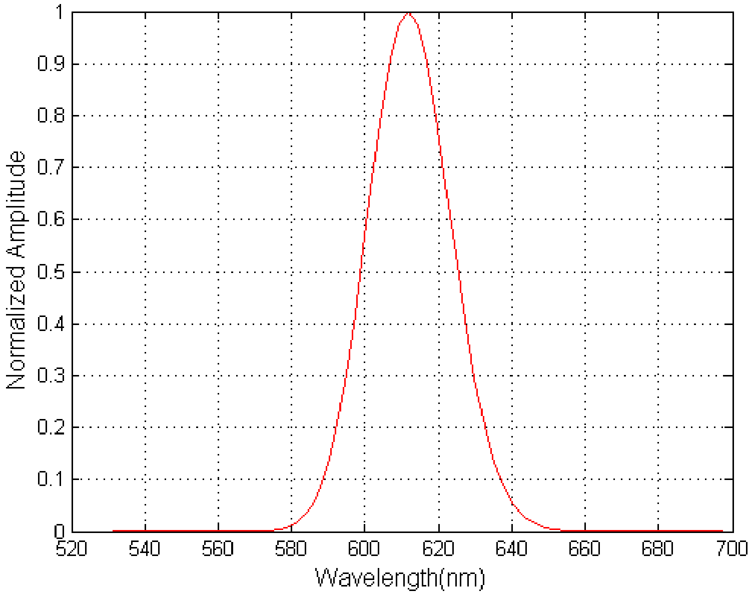

Figure 4-11 Spectrum of the emitter

The following Figure 4-12 shows the normalized time domain magnetic field of the emitter

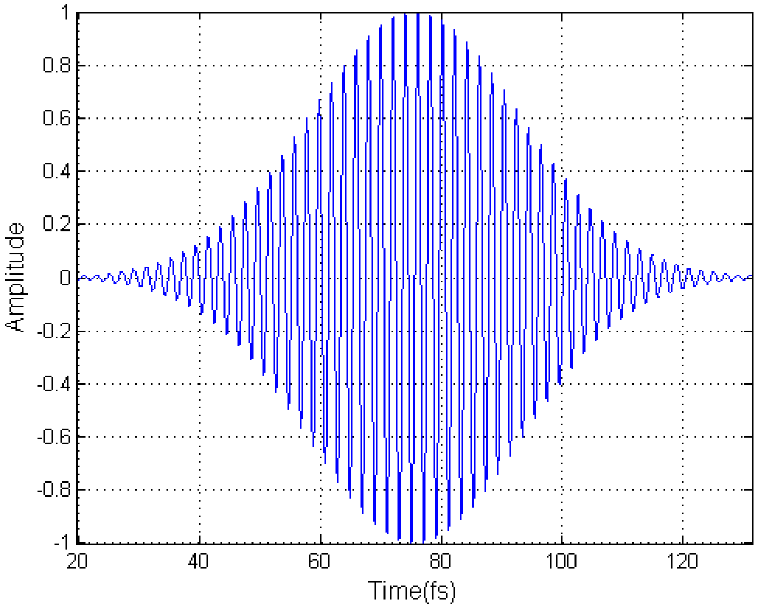

Figure 4-12 Emitter in time domain

4.3.1 Results for Fixed Bio-material Thickness

For bio-sensing the average intensity enhancement is found in the region very close to the nano-particles. Average intensity enhancement is defined as the ratio of average intensity in an area very close to the particles (within the red-dashed rectangular region in Figure 4-9) to the average intensity in the same region without the nanoparticles as

$$Average\ Intensity\ Enhancement = \frac{\int I_{ave,with\ particles}}{\int I_{ave,without\ particles}} \qquad 4.4$$

The dipoles are placed at an optimum distance (d in Figure 4-9) of the nanoparticles where the intensity enhancement is maximum. From the figure it is seen that the optimum distance is found to be $27nm$ where the intensity enhancement is maximum.

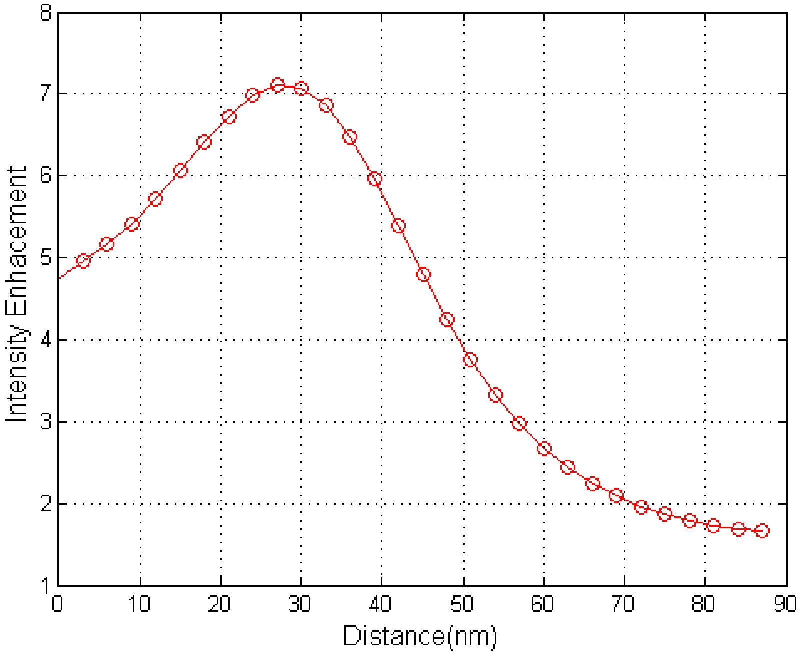

Figure 4-13 Average Intensity Enhancement vs Distance.

With the distance between the nanoparticles and source optimized the refractive index of the bio-material (Figure 4-9) is varied first in steps of 0.01 RIU then in steps of 0.1.The thickness of the bio-material material is $20nm$. This variation in the refractive index takes the nano-particles out of resonance there is a fall in the average intensity enhancement as shown in Figure 4-14.

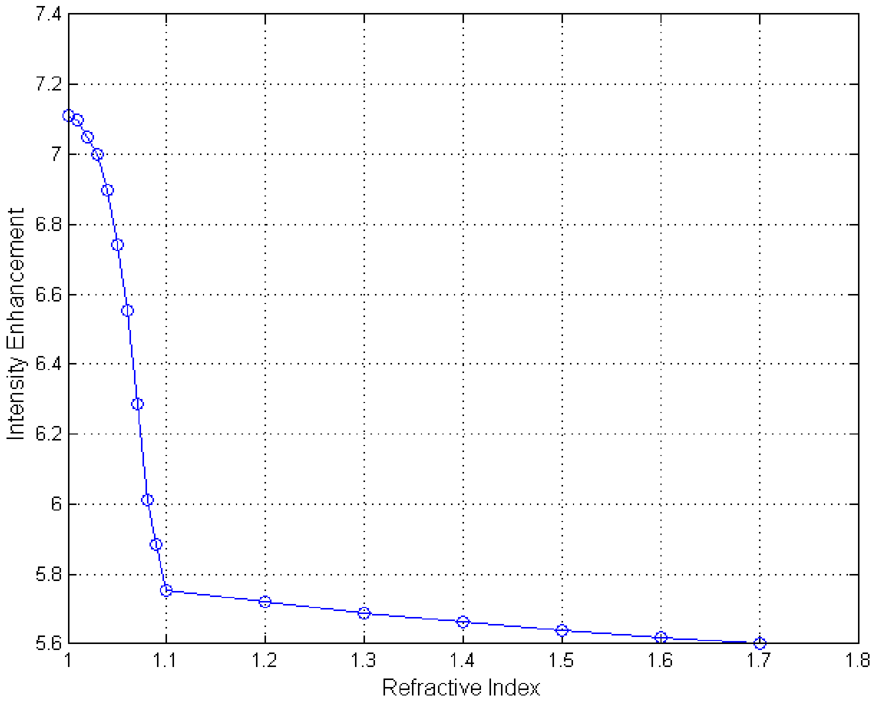

Figure 4-14 Intensity Enhancement vs Refractive index of bio-material.

When the nano-particles are out of resonance there is a very small change in the average intensity as the device is out of resonance with change in refractive index.

4.3.2 Results for Varying Bio-Material Thickness

The variation in enhancement intensity is also investigated by fixing the refractive index of the material and varying the thickness of the bio-material.

The first numerical experiment in this case is done by fixing the refractive index at 1.1 and increasing the thickness from $0nm$ (no-biomaterial) to $50nm$. It is seen from Figure 4-15 that the intensity enhancement decreases and then there is very small decrease after $40nm$. The effect of thickness is of the biomaterial becomes minimal when the thickness of the material is above the penetration depth of the surface plasmons that are excited on the nano-particles.

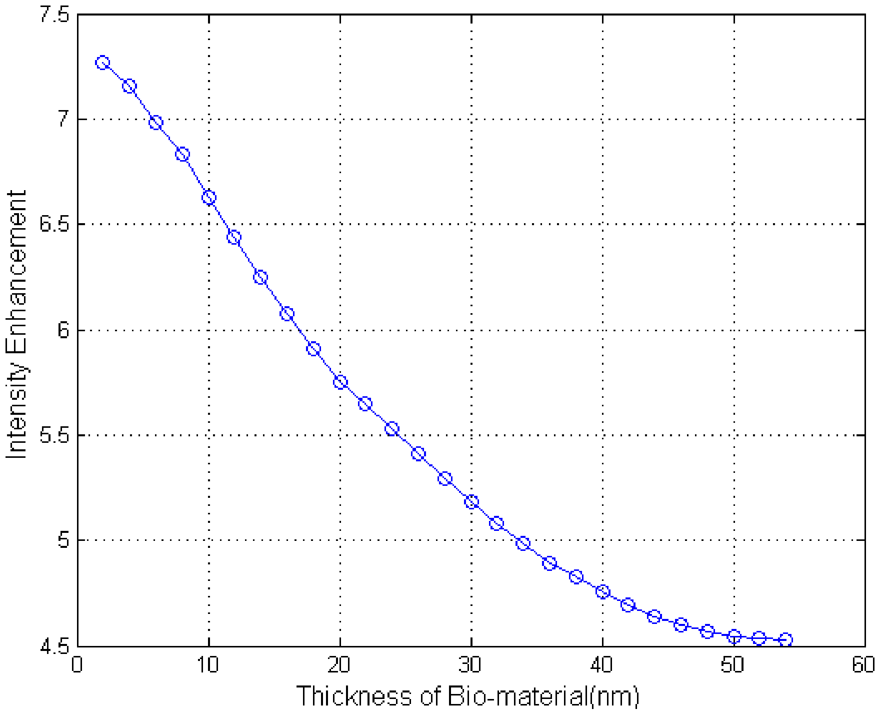

Figure 4-15 Intensity Enhancement vs Thickness of biomaterial

Another numerical investigation was done for a refractive index of the bio-material at 1.06. As seen from Figure 4-16 that the drop in intensity enhancement is slower for case of refractive index of bio-material 1.06. The intensity enhancement change is slower when than when the refractive index is at 1.1 and the drop in enhancement becomes smaller and smaller until it becomes nearly constant as seen in Figure 4-16. This happens because with refractive index 1.06 the device is still under resonance condition. Only when it is completely off-resonance the intensity decreases faster that is when the refractive index is at 1.1.

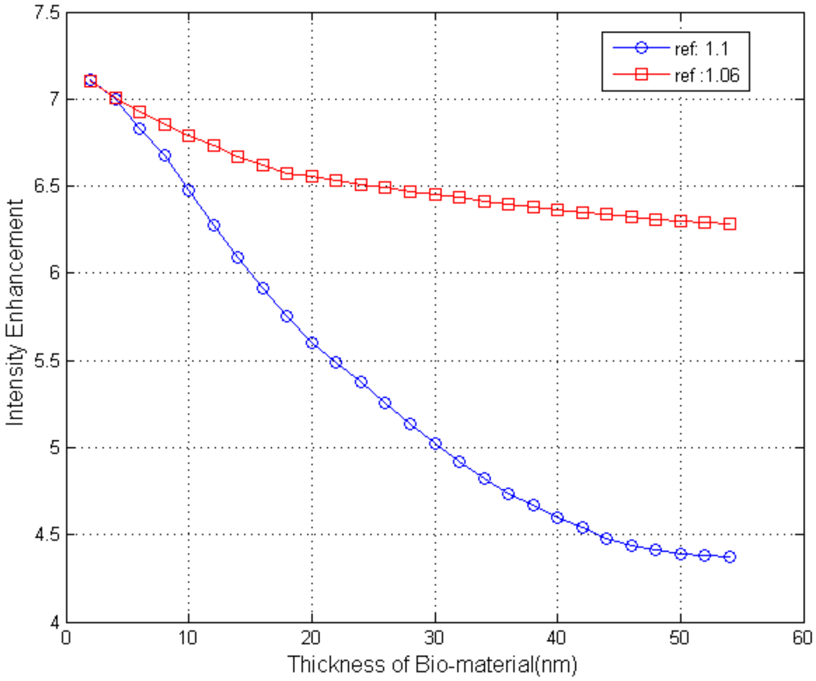

Figure 4-16 Intensity Enhancement vs Thickness of Biomaterial for two different refractive indices 1.1 and 1.06

4.3.3 Scattering Properties

The scattering cross-section with varying refractive index of the bio-material was also found as seen in Figure 4-17 there is a shift in the spectrum. This confirms that there is change in resonance conditions with change in the bio-material layer's refractive index.

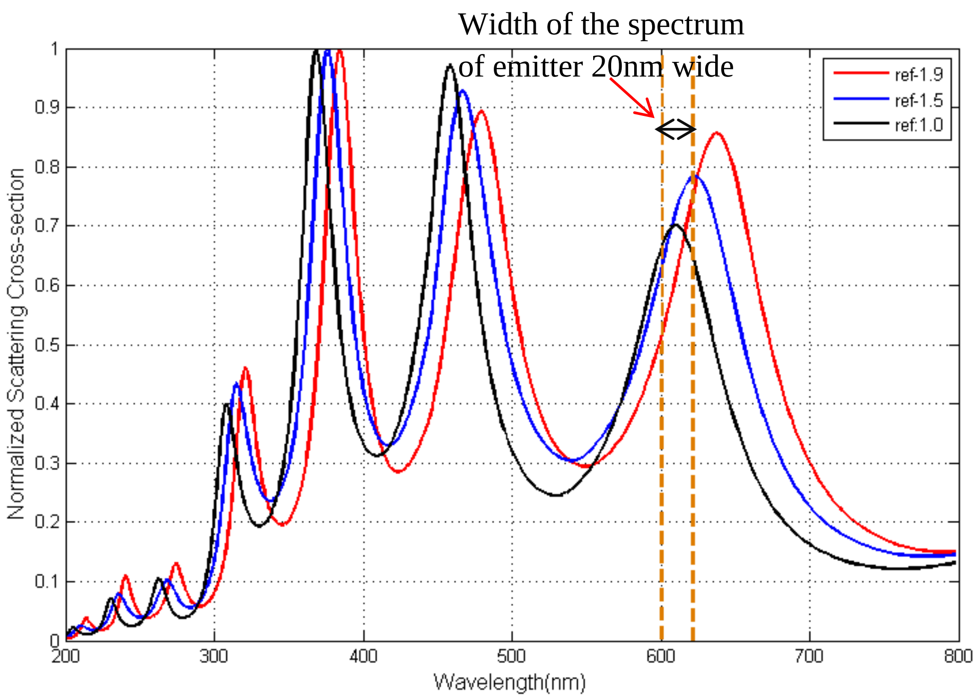

Figure 4-17 Scattering cross-section of varying bio-material refractive index (1.0, 1.5 and 1.9)

There is a considerable shift in the scattering spectrum of the device which changes with the refractive index. Note the emission bandwidth of the emitter when compared to the particles response.

Using the scattering cross-section sensitivity of the device can be found. The change in wavelength from refractive index 1.0 to 1.9 is $28.9nm$ this translates to sensitivity of $31.7778nm/RIU$

4.3.4 Real-Time Binding

Another computational experiment had been done to test the real-time binding of bio-material. In this test the refractive index of the bio-material is fixed and to simulate binding non-uniformly bio-material is made to appear in $20nm$ thick and $20nm$ wide 'islands' of refractive index 1.1 with time until the whole sensing region is filled with a $20nm$ thick uniform layer of bio-material with refractive index 1.1. Figure 4-18 shows the response of intensity enhancement with time. The ‘islands’ appear with time in a deterministic manner with first ‘island’ appearing in the center of the sensing area and then symmetrically appearing outwardly to form a uniform layer of bio-material $20nm$ thick. There is a linear drop in the intensity enhancement until the time the localized surface plasmon is influenced by the appearance of ‘islands’ and then there is almost no change in the intensity enhancement.

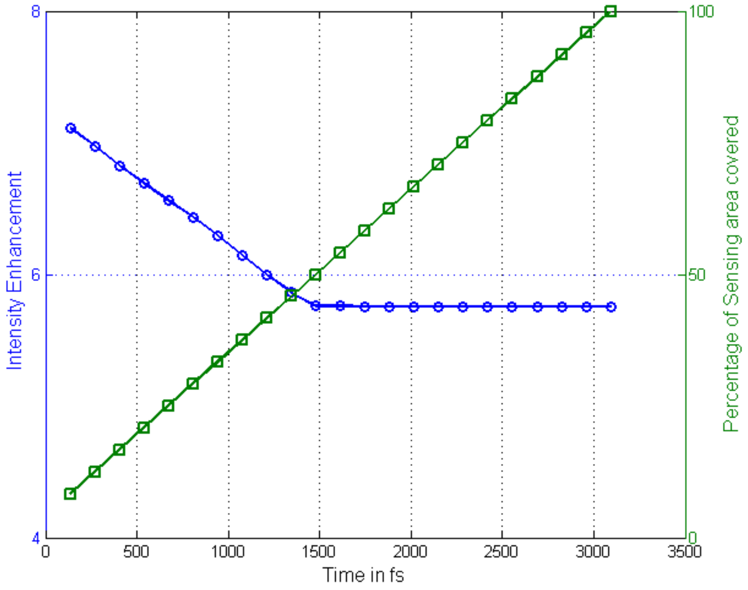

Figure 4-18 Real time sensing

Summary and discussions

A device based on nanoparticles coupled to an emitter has been designed and its response to changing bio-material refractive index is investigated.

- A very narrow band emitter is used for sensing which is similar to the emission spectrum of Eu^{3+} and the average enhancement intensity has been calculated.

- The average enhancement intensity is dependent on the distance that the emitter is from the nanoparticles and it is found to be maximum at $27nm$ from the nanoparticles.
- When the bio-material's refractive index is changed from 1.0 to 1.1 it goes off resonance and there is a sharp fall in the average enhancement intensity
- The emission spectrum of the source is sharp and combined with nanoparticles resonance condition this decrease in average intensity enhancement is very sharp.
- It is also noted that the average enhancement intensity does not change considerably when it leaves the resonance condition.
- When it is at a refractive index of 1.1 with increasing thickness the average intensity enhancement decreases and then stabilizes this is due to the penetration of the field due to surface plasmon in the bio material is small and with increasing thickness there is very less change in the average intensity enhancement.
- With a refractive index of 1.06 the intensity enhancement decreases slowly than when it is 1.1 it is due to the device still being in resonance
- So in conclusion the multiple sensitivities of the emitter and plasmonic particles have been utilized for sensing.

Chapter 5

SUMMARY AND CONCLUSIONS

5.1 Summary

This thesis investigated the various devices based on nano-scale plasmonic resonators for the application to bio-sensing. To simulate such structures silver was chosen as the plasmonic metal. Silver was modeled and included in the FDTD simulator using the general ADE FDTD algorithm. The research done in this thesis is summarized as follows.

- Dispersive material model was incorporated into the FDTD algorithm using the general ADE FDTD algorithm.
- A dispersive model of silver using the 6-pole Lorentz-Drude model was used to simulate the frequency dependent behavior of silver in the optical wavelength ranges was used in the simulator.
- An M-I-M waveguide coupled Metal-Insulator-Metal ring resonator was modeled and its transmittance properties calculated. This device is also investigated for its sensing properties. The sensitivity of the device, Figure of Merit and Limit of Detection is calculated.
- Another M-I-M waveguide coupled Metal–Insulator-Metal ring resonator with grating in the core is investigated for different period of the grating in the core. Two grating based MIM devices are investigated using two different period of 45^o and 90^o are investigated for sensing. The devices' sensitivity, Figure of Merit and Limit of detection are calculated.

- A device based on silver nano-particles is also investigated in this thesis. First the particle configuration is optimized such that it matches the wavelength of the emitter and is sharp enough.
- Then dipole emitters are used to optimize the distance at which the emitters are to be placed for maximum intensity enhancement and it is investigated for its sensing properties for varying refractive index, varying thickness simulating binding and real-time sensing capability.

5.2 Conclusions

In conclusion the two types of devices based on plasmonic resonators have been tested

- It is concluded from the above results that the simple M-I-M ring resonator has very high sensitivity to refractive index changes and this sensitivity increases with increasing size of the ring and also with decreasing width of the ring. There is also a decrease in the FWHM values of the device with increasing width. These variations in sensitivity and FWHM make the device have FOM values that improve with size and width of the ring.
- When a grating is introduced in the MIM ring there is a complete transformation in the transmittance spectrum of the ring and the device becomes extremely tunable. It was seen that with introduction of grating and a slot for sensing, the sensitivity of the device reaches a maximum value and also sensitivity increases with decreasing size of the ring and this in turn has an effect on the FOM of the device giving maximum FOM values for smaller size of the device. And also with introduction of grating larger wavelengths (optical wavelengths) are now resonant modes of the device with smaller radius compared to the simple ring.

So it can be concluded that grating introduces a method of controlling the resonant modes of the plasmonic ring resonator and also has an effect on the performance of the device which helps in reducing the size but with improved sensitivity parameters.

- The second type of device that is tested is the nano-particle based sensor. It has been found that plasmonic nano-particles if coupled to an emitter can be used as a sensor utilizing the multiple sensitivities of the both the particles' resonant characteristics and also the sharp response of the emitter.

5.3 Future Work

The final frontier in bio-sensing is single molecule sensing and the obvious future work that can be suggested is to design devices that are more sensitive and are able to sense even the smallest changes in refractive index. Specific suggestions for future work may be as follows

- The M-I-M ring resonator can be investigated with periodic boundary conditions or an array.
- M-I-M ring can also be used in conjunction with active material and can be used for sensing with an aim of reducing the complexity in practical implementations.
- In the nano-particle based resonator various other shapes of nanoparticles which have sharper responses can be investigated thus making the device more sensitive.
- This work can also be extended to 3-D domain so as to give more realistic results.

References

[1] H. Raether, *Surface Plasmons on smooth and rough surfaces and on gratings*. Springer-Verlag, 1986.

[2] T. . W. Ebbesen, H. . J. Lezec, H. F. Ghaemi, T. Thio, and P. . A. Wolff, “Extraordinary optical transmission through subwavelength hole arrays,” *Lett. To Nat.*, vol. 391, no. 6, p. 667, Mar. 1998.

[3] J. Pendry, “Negative refraction makes a perfect lens,” *Phys. Rev. Lett.*, vol. 85, no. 18, pp. 3966–9, Oct. 2000.

[4] M. M. Cox, J. Doudna, and M. O’Donnell, *Molecular Biology*. W H Freeman, 2012.

[5] K. M. Mayer and J. H. Hafner, “Localized Surface Plasmon Resonance Sensors,” *Chem. Rev.*, vol. 111, pp. 3828–3857, 2011.

[6] S. A. Maier, *Plasmonics:Fundamentals and Applications*, 2007th ed. Springer, 2007.

[7] V. Myroshnychenko, J. Rodríguez-Fernández, I. Pastoriza-Santos, A. M. Funston, C. Novo, P. Mulvaney, L. M. Liz-Marzán, and F. J. García de Abajo, “Modelling the optical response of gold nanoparticles.,” *Chem. Soc. Rev.*, vol. 37, no. 9, pp. 1792–805, Sep. 2008.

[8] C. F. Bohren and D. R. Huffman, *Absorption and Scattering of Light by small nano particles*, vol. 77, no. 6. Wiley-Interscience Publications, 1983.

[9] M. Alam, S. Member, and Y. Massoud, “A Closed-Form Analytical Model for Single Nanoshells,” *IEEE Transscations Nanotechnol.*, vol. 5, no. 3, pp. 265–272, 2006.

[10] H. Wang, D. W. Brandl, F. Le, P. Nordlander, and N. J. Halas, “Nanorice: a hybrid plasmonic nanostructure.,” *Nano Lett.*, vol. 6, no. 4, pp. 827–32, Apr. 2006.

[11] F. Hao, Y. Sonnefraud, P. Van Dorpe, S. a Maier, N. J. Halas, and P. Nordlander, “Symmetry breaking in plasmonic nanocavities: subradiant LSPR sensing and a tunable Fano resonance.,” *Nano Lett.*, vol. 8, no. 11, pp. 3983–8, Nov. 2008.

[12] B. Luk’yanchuk, N. I. Zheludev, S. a Maier, N. J. Halas, P. Nordlander, H. Giessen, and C. T. Chong, “The Fano resonance in plasmonic nanostructures and metamaterials.,” *Nat. Mater.*, vol. 9, no. 9, pp. 707–15, Sep. 2010.

[13] L. J. Sherry, S. Chang, G. C. Schatz, R. P. Van Duyne, B. J. Wiley, and Y. Xia, “Localized Surface Plasmon Resonance Spectroscopy of Single Silver Nanocubes,” *Nano Lett.*, vol. 5, no. 10, pp. 2034–2038, 2005.

[14] F. Tam, “Optimization of Nanoshell geometry for Plasmon enhanced Flouresence,” Rice University, 2007.

[15] E. M. Larsson, J. Alegret, M. Käll, and D. S. Sutherland, “Sensing characteristics of NIR localized surface plasmon resonances in gold nanorings for application as ultrasensitive biosensors.,” *Nano Lett.*, vol. 7, no. 5, pp. 1256–63, May 2007.

[16] R. Bukasov and J. S. Shumaker-Parry, “Highly tunable infrared extinction properties of gold nanocrescents.,” *Nano Lett.*, vol. 7, no. 5, pp. 1113–8, May 2007.

[17] C. L. Nehl, H. Liao, and J. H. Hafner, “Optical properties of star-shaped gold nanoparticles.,” *Nano Lett.*, vol. 6, no. 4, pp. 683–8, Apr. 2006.

[18] J. B. Jackson, S. L. Westcott, L. R. Hirsch, J. L. West, and N. J. Halas, “Controlling the surface enhanced Raman effect via the nanoshell geometry,” *Appl. Phhysics Lett.*, vol. 257, p. 257, 2003.

[19] H. Wang, J. Kundu, and N. J. Halas, “Plasmonic nanoshell arrays combine surface-enhanced vibrational spectroscopies on a single substrate.,” *Angew. Chem. Int. Ed. Engl.*, vol. 46, no. 47, pp. 9040–4, Jan. 2007.

[20] B. Luk’yanchuk, N. I. Zheludev, S. a Maier, N. J. Halas, P. Nordlander, H. Giessen, and C. T. Chong, “The Fano resonance in plasmonic nanostructures and metamaterials.,” *Nat. Mater.*, vol. 9, no. 9, pp. 707–15, Sep. 2010.

[21] H. Lu, X. Liu, D. Mao, and G. Wang, “Plasmonic nanosensor based on Fano resonance in waveguide-coupled resonators.,” *Opt. Lett.*, vol. 37, no. 18, pp. 3780–2, Sep. 2012.

[22] B. Hecht, P. Mühlschlegel, J. N. Farahani, H.-J. Eisler, D. W. Pohl, O. J. F. Martin, and P. Biagioni, “Prospects of Resonant Optical Antennas for Nano-Analysis,” *Chim. Int. J. Chem.*, vol. 60, no. 11, pp. 765–769, Nov. 2006.

[23] R. Vogelgesang, W. Khunsin, C. Rockstuhl, C. Etrich, and K. Kern, “Plasmonic Nanowire Antennas : Experiment , Simulation , and Theory,” *Nano Lett.*, vol. 10, pp. 3596–3603, 2010.

[24] P. Bharadwaj, B. Deutsch, and L. Novotny, “Optical Antennas,” *Adv. Opt. Photonics*, vol. 1, pp. 438–483, 2009.

[25] P. Nordlander, “The ring: a leitmotif in plasmonics.,” *ACS Nano*, vol. 3, no. 3, pp. 488–92, Mar. 2009.

[26] I. Zand, M. S. Abrishamian, and P. Berini, “Highly tunable nanoscale metal-insulator-metal split ring core ring resonators (SRCRRs),” *Opt. Express*, vol. 21, no. 1, p. 79, Jan. 2013.

[27] T. D. Corrigan, P. W. Kolb, a B. Sushkov, H. D. Drew, D. C. Schmadel, and R. J. Phaneuf, “Optical plasmonic resonances in split-ring resonator structures: an improved LC model.,” *Opt. Express*, vol. 16, no. 24, pp. 19850–64, Nov. 2008.

[28] I. Zand, A. Mahigir, T. Pakizeh, and M. S. Abrishamian, “Selective-mode optical nanofilters based on plasmonic complementary split-ring resonators.,” *Opt. Express*, vol. 20, no. 7, pp. 7516–25, Mar. 2012.

[29] B. Lahiri, A. Z. Khokhar, R. M. D. La Rue, S. G. Mcmeekin, and N. P. Johnson, “Asymmetric split ring resonators for optical sensing of organic materials,” vol. 17, no. 2, pp. 1107–1115, 2009.

[30] H. Jiang and J. Sabarinathan, “Effects of Coherent Interactions on the Sensing Characteristics of Near-Infrared Gold Nanorings,” *J. Phys. Chem. C*, vol. 114, no. 36, pp. 15243–15250, Sep. 2010.

[31] D. F. P. Pile and D. K. Gramotnev, “New Plasmonic Sub-wavelength waveguides:Next to zero losses at sharp bends,” *Opt. Lett.*, vol. 30, no. 10, pp. 1186–1188, 2005.

[32] J. A. Dionne, L. A. Sweatlock, and H. A. Atwater, “Plasmon slot waveguides : Metal-Insulator-Metal (MIM),” *Phys. Rev. B*, vol. 73, 2006.

[33] N. Talebi, A. Mahjoubfar, and M. Shahabadi, “Plasmonic ring resonator,” *J.Opt. Soc.Am.B*, vol. 25, no. 12, pp. 2116–2122, 2008.

[34] A. Hosseini and Y. Massoud, “Nanoscale surface plasmon based resonator using rectangular geometry Nanoscale surface plasmon based resonator using rectangular geometry,” vol. 181102, no. 2007, 2012.

[35] Z. Huawei, H. Xuguang, and H. Jingtang, “Surface plasmon polaritons based optical directional coupler,” *Sci. China Ser. G*, vol. 51, no. 07117866, pp. 1877–1882, 2008.

[36] A. Setayesh, S. R. Mirnaziry, and M. S. Abrishamian, “Numerical Investigation of Tunable Band-pass \ band-stop Plasmonic Filters with Hollow-core Circular Ring Resonator,” *J. Opt. Soc. Korea*, vol. 15, no. 1, pp. 82–89, 2011.

[37] L. Novotny, B. Hecht, and D. W. Pohl, “Interference of locally excited surface plasmons,” *J. Appl. Phys.*, vol. 81, no. 4, 1997.

[38] P. Anger, P. Bharadwaj, and L. Novotny, “Enhancement and Quenching of Single-Molecule Fluorescence,” *Phys. Rev. Lett.*, vol. 96, no. 11, p. 113002, Mar. 2006.

[39] H. Nabika and S. Deki, “Enhancing and Quenching Functions of Silver Nanoparticles on the Luminescent Properties,” vol. 107, no. 35, pp. 8–11, 2003.

[40] V. Giannini, A. I. Fernández-Domínguez, S. C. Heck, and S. a Maier, “Plasmonic nanoantennas: fundamentals and their use in controlling the radiative properties of nanoemitters.,” *Chem. Rev.*, vol. 111, no. 6, pp. 3888–912, Jun. 2011.

[41] M. Ambati, D. a. Genov, R. F. Oulton, and X. Zhang, “Active Plasmonics: Surface Plasmon Interaction With Optical Emitters,” *IEEE J. Sel. Top. Quantum Electron.*, vol. 14, no. 6, pp. 1395–1403, 2008.

[42] F. Kaminski, V. Sandoghdar, and M. Agio, “Finite Difference Time Domain Modelling of Decay Rated in the Near Field of Metal Nanostrucutres,” *J. Comput. Theor. Nanosci.*, vol. 4, pp. 635–643, 2007.

[43] K. J. Russell, T. Liu, S. Cui, and E. L. Hu, “Large spontaneous emission enhancement in plasmonic nanocavities,” *Nat. Photonics*, vol. 6, no. July, pp. 2–5, 2012.

[44] K. S. Yee, “Numerical Solution of Initial Boundary Value Problems Involving Maxwell’s Equations in Isotropic Media,” *IEEE Transscations Antennas Propag.*, 1966.

[45] M. Futamata, Y. Maruyama, and M. Ishikawa, “Local Electric Field and Scattering Cross Section of Ag Nanoparticles under Surface Plasmon Resonance by Finite Difference Time Domain Method,” *J. Phys. Chem. B*, vol. 107, no. 31, pp. 7607–7617, Aug. 2003.

[46] C. Oubre and P. Nordlander, “Optical Properties of Metallodielectric Nanostructures Calculated Using the Finite Difference Time Domain Method,” *J. Phys. Chem. B*, vol. 108, no. 46, pp. 17740–17747, Nov. 2004.

[47] G. Mur, “Absorbing Boundary Conditions for the Finite-Difference Approximation of the Time-Domain Electromagnetic-Field Equations,” *IEEE Trans. Electromagn. Compat.*, vol. EMC-23, no. 4, pp. 377–382, Nov. 1981.

[48] K. L. Shlager and J. B. Schneider, “A selective survey of the finite-difference time-domain literature,” *IEEE Antennas Propag. Mag.*, vol. 37, no. 4, pp. 39–57, 1995.

[49] A. Taflove and S. C. Hagness, *Computational Electrodynamics,* Third Edition. Artech House, 2005.

[50] K. Umashankar and A. Taflove, “A Novel Method to Analyze Electromagnetic Scattering of Complex Objects,” *IEEE Trans. Electromagn. Compat.*, vol. EMC-24, no. 4, pp. 397–405, Nov. 1982.

[51] Z. L. He, K. Huang, Y. Zhang, Y. Yan, and C. H. Liang, “Study on High Performance of MPI-Based Parallel FDTD from WorkStation to Super Computer Platform,” *Int. J. Antennas Propag.*, vol. 2012, pp. 1–7, 2012.

[52] A. Taflove and S. C. Hagness, *Computational Electrodynamics,* Third Edit. Artech House, 2005.

[53] M. A. Alsunaidi and A. A. Al-jabr, “A General ADE-FDTD Algorithm for the Simulation of Dispersive Structures,” *IEEE Photonics Technol. Lett.*, vol. 21, no. 12, pp. 817–819, 2009.

[54] A. B. Djuris, J. M. Elazar, and M. L. Majewski, “Optical properties of metallic films for vertical-cavity optoelectronic devices,” *Appl. Opt.*, vol. 37, no. 22, pp. 5271–5283, 1998.

[55] J.-P. Berenger, “A Perfectly Matched Layer for the Absorption of Electromagnetic Waves,” *J. Comput. Phys.*, vol. 114, pp. 185–200, 1994.

[56] A. P. Zhao, M. Ieee, J. Juntunen, and V. R. Antti, “Generalized Material-Independent PML Absorbers for the FDTD Simulation of Electromagnetic Waves in Arbitrary Anisotropic Dielectric and Magnetic Media,” *IEEE Microw. Guid. Wave Lett.*, vol. 8, no. 2, pp. 52–54, 1998.

Vitae

Name : Mohammed Tayyab Mohi Mujahid

Nationality : Indian

Date of Birth : 10/26/1988

Email : g201101790@kfupm.edu.sa, tayyab.mujahid@gmail.com

Address :Hno 11-3-726, New Mallepally, Hyderabad .India 500001

Academic Background : MS in Electrical Engineering (Major: Electromagnetics)
KFUPM, Dhahran 2013
BE in Electronics and Communications,
Osmania University 2010